Engineering with Computers
https://doi.org/10.1007/s00366-025-02178-0

ORIGINAL ARTICLE

A novel smooth particle hydrodynamics framework for modelling melting pool dynamics in laser processing

Zhihao Zhong[1] · **Sivakumar Kulasegaram**[1] · **Emmanuel Brousseau**[1]

Received: 8 February 2025 / Accepted: 25 June 2025

Abstract
Accurately modelling melting pool dynamics, including surface tension and Marangoni force, is essential for reliable numerical investigations of laser material processing operations. However, conventional Smooth Particle Hydrodynamics (SPH) approaches often struggle to estimate these forces due to the truncated kernel support and unified kernel partition. To address these limitations, a novel geometry-based scheme was proposed for the estimation of surface tension and Marangoni force. Using numerical benchmarks, the initial comparison of the developed scheme against conventional approaches revealed that the proposed framework could be more accurate, particularly in estimating the surface curvature and surface temperature gradient. Following these validations, the proposed framework was applied to model two different laser material processing operations, namely laser micro texturing and laser powder bed fusion (LPBF). In the simulations conducted for laser micro texturing, the Marangoni force and surface tension were found to be the primary factors influencing the generation of textured patterns. Furthermore, the simulated melt pool shape and surface profile demonstrated good agreement with experiments. When implemented for LPBF, the proposed framework was shown to produce numerically stable outcomes and the simulated melt depth also demonstrated reasonably good agreement with experimental data. Based on the obtained results, it is argued that the proposed SPH scheme can offer an accurate numerical framework for modelling melting pool dynamics for a wide range of laser material processing applications.

Keywords Laser micro texturing · Laser powder bed fusion · SPH · Melting pool dynamics · Surface tension · Marangoni force

1 Introduction

Smooth Particle Hydrodynamics is a mesh-free, Lagrangian-based numerical method initially proposed by Lucy [1] and Gingold and Monaghan [2] to investigate astrophysical phenomena in the free boundary domain. Over the past three decades, SPH has been extensively applied to a wide range of engineering problems due to its distinct features. First, SPH is known for its advantage in handling multiple coupling and free surface flow [3, 4]. Indeed, with more traditional mesh-based methods, additional numerical treatments are typically required to address the numerical issues associated with large deformation and free surface flow. Given that SPH is a pure mesh-free method, the need of such treatments is eliminated, thereby simplifying the modelling process. In addition to its mesh-free nature, SPH is a Lagrangian-based numerical method, which provides a distinct advantage in tracking specific material points throughout the simulation [4]. In the past decades, the low computational efficiency of SPH may have limited its applications to engineering problems. However, recent advancements in computer hardware and GPU acceleration have significantly enhanced its computational potential [3, 5, 6]. For these reasons, SPH has increasingly been recognised as an effective and promising numerical tool for simulating laser processing in recent years [3]. In particular, a number of 2D and 3D SPH models were developed to study the evolution of the laser powder bed fusion process [4–12]. In addition to additive manufacturing, laser welding, laser drilling and laser ablation have also been recently modelled using the SPH method [13–16]. Some encouraging simulation results were obtained from the reported SPH models in this body of literature.

✉ Sivakumar Kulasegaram
kulasegarams@cardiff.ac.uk

[1] School of Engineering, Cardiff University, Cardiff, UK

Published online: 16 July 2025

Laser micro texturing is a relatively new laser material processing technology, which can be applied to modify the wettability of metallic alloys, such as enhancing the hydrophilicity or hydrophobicity of surfaces as a function of the textured patterns [17, 18]. Therefore, predicting the surface topography generated by laser micro texturing has attracted the interest from research community. In this context, Melo-Fonseca et al. developed a regression model based on the experimentally measured patterns [19]. Although this model could provide insights into the textured patterns in their conducted experiments, it may not be completely appropriate for predicting the textured patterns under varying experimental conditions. In addition to this approach, Zhang et al. developed a mesh-based numerical model of laser micro texturing using the commercial software COMSOL [20]. These authors found that the recoil pressure plays an essential role in the generation of textured surface patterns. However, the Marangoni force was not considered in the developed model, which could have an impact on the accuracy of the results and may not fully reflect realistic processing conditions.

Laser powder bed fusion (LPBF) is one of the most common additive manufacturing techniques, renowned for its distinct advantages in fabricating complex-shaped parts with high resolution and accuracy [21, 22]. For this reason, various numerical models have been developed to understand the physical phenomenon of LPBF and to predict several experimental outcomes [23]. In the context of particle-based simulations of LPBF, Russell et al. developed a 2D SPH model that demonstrated the potential of this modelling approach for LPBF [4]. However, it is argued that the numerical scheme employed in their study for modelling melting pool dynamics could be further refined to increase its accuracy. Long et al. developed SPH models of LPBF using an improved kernel gradient correction approach [10, 11]. This approach demonstrated superior simulated outcomes compared to conventional methods in the conducted test cases. Nevertheless, the accuracy of the reported models may be limited due to the low particle resolution used in the simulations. Indeed, the low computational efficiency of SPH could restrict its application in LPBF to some extent. Consequently, developing the GPU-accelerated frameworks has garnered great interest from research community [5, 6, 12].

The surface tension and Marangoni force are commonly regarded as fundamental components of the melting pool dynamics. However, modelling such surface forces with SPH could encounter some challenges. Firstly, the approximation of surface tension force involves the estimation of curvature, and numerical corrections are necessary to enhance accuracy and reliability of the estimated curvature [24, 25]. In addition, the approximation of Marangoni force requires the estimation of surface tangential temperature gradient [26]. Due to the truncated kernel support of the surface particles and the unified partition of smoothing kernel, using the conventional kernel gradient approximation to estimate the surface tangential temperature gradient could be ill-suited.

To overcome the limitations of these conventional SPH approaches, a novel scheme is proposed in this study, for which the surface curvature and surface temperature gradient are estimated using interpolation and geometric relationships of surface particles. In addition, the proposed framework for modelling melting pool dynamics incorporates a grid-based laser source absorption scheme, velocity damping of phase transformation, an enhanced particle shifting technique and barrier forces. Numerical validations were firstly conducted to verify the accuracy of the developed scheme for modelling surface tension and surface temperature gradient. Following the successful implementation of validation tests, the framework was applied to specific laser material processing applications. Due to the lack of particle-based numerical investigations in laser micro texturing, the proposed framework was applied to model this specific process and explore the potential of this particle-based modelling scheme. The simulated micro texture profiles were validated by comparing them with experimental data available from the literature for which Ti6Al4V had been employed [27, 28]. To further verify its accuracy and potential application to other laser material processing techniques, the framework was subsequently employed to model the LPBF process. In this case, the simulated melt depth was compared with experimental data obtained from the literature, where 316 L stainless steel was used [29].

2 Methodology

2.1 Smooth particle hydrodynamics

In this section, a brief description of the SPH method is presented. The computational domain in SPH consists of a set of particles, each assigned certain physical properties, such as position, velocity and mass. The interactions among particles are controlled by the discrete SPH form of governing equations within the range of the smoothing length.

Through the kernel approximation and particle approximation, a given continuous function $f(\boldsymbol{r})$ can be transformed into a fundamental SPH discretisation form [30]. With the kernel approximation, the integral and rigorous smoothing form of a function,

$$f(\boldsymbol{r}) = \int \delta\ (\boldsymbol{r} - \boldsymbol{r'})\, f(\boldsymbol{r'})\, d\boldsymbol{r'}, \tag{1}$$

is converted into a finite form via replacing the Dirac delta function $\delta(\boldsymbol{r}-\boldsymbol{r'})$ by a smoothing function, $W(\boldsymbol{r}-\boldsymbol{r'},h)$, as expressed below:

$$f(\boldsymbol{r}) = \int W(\boldsymbol{r}-\boldsymbol{r'},h)\, f(\boldsymbol{r'})\, d\boldsymbol{r'}, \tag{2}$$

where, $\boldsymbol{r}$ represents the position vector, and h denotes the smoothing length, which is used to determine the influence of each particle on its surrounding particles based on their inter-particle distances. Next, the continuous form of the kernel approximation of a function is transferred into a discrete summation over the neighbouring particles through the particle approximation, as expressed:

$$f(\boldsymbol{r}_i) = \sum_j^N W_{ij} f(\boldsymbol{r}_j) \frac{m_j}{\rho_j}, \tag{3}$$

where N is the total number of neighbouring particles, $W_{ij} = W(\boldsymbol{r}_{ij},h)$ is the smoothing function ($\boldsymbol{r}_{ij} = \boldsymbol{r}_i - \boldsymbol{r}_j$), and m_j and ρ_j are the mass and density of the neighbouring particles, respectively. Through the kernel and particle approximations, the SPH form of governing equations of specific engineering problems can be derived. A more comprehensive introduction of the SPH methodology can be found in [30].

2.2 Computational model for fluid dynamics

Fluid dynamics are governed by the Navier-Stokes equations on a Lagrangian frame. In this study, the δ-SPH scheme [31] and particle shifting technique [32] were employed to enhance the numerical solutions. Consequently, the fluid dynamics of a SPH particle i under the influence of particle j in the support domain can be approximated as follows:

$$\begin{cases} \frac{d\rho_i}{dt} = \rho_i \sum_j u_{ij} \cdot \nabla_i W_{ij} V_j + \delta c_0 h \sum_j Y_{ij} \cdot \nabla_i W_{ij} V_j, \\ \frac{du_i}{dt} = -\sum_j \frac{1}{\rho_i}(p_i + p_j)\nabla_i W_{ij} V_j \\ \qquad + \sum_j \frac{1}{\rho_i}\left(\frac{2\mu_i\mu_j}{\mu_i+\mu_j}\right)\pi_{ij}\nabla_i W_{ij} V_j + g + \frac{b_i}{\rho_i} \\ \frac{dr_i}{dt} = u_i, \quad r_i' = r_i + \delta r_i, \qquad p_i = c_0^2(\rho_i - \rho_0), \end{cases} \tag{4}$$

where $\boldsymbol{u}_{ij} = \boldsymbol{u}_i - \boldsymbol{u}_j$,$\boldsymbol{u}_i$ and $\boldsymbol{u}_j$ are the velocity of particle i and j, δ is the δ-SPH smoothing parameter, c_0 is the artificial sound speed, h is the smoothing length, $V_j = m_j/\rho_j$ is the volume of particle j, ρ_i and $\rho_j$are the density of particle i and j, p_i and p_j are the pressure, μ_i and μ_j are the viscosity, $\boldsymbol{g}$ is the gravity, $\boldsymbol{b}_i$ represents any other body forces acting on particle i, $\delta\boldsymbol{r}_i$ is the shifting distance introduced by the particle shifting technique (see the subsequent Sect. 2.5.1), ρ_0 is the reference density, and π_{ij} is the viscosity term given by [33]:

$$\pi_{ij} = 2(n_D+2)\frac{\boldsymbol{u}_{ij}\cdot\boldsymbol{r}_{ij}}{|\boldsymbol{r}_i - \boldsymbol{r}_j|^2}, \tag{5}$$

where n_D is the dimension factor. Additionally, in Eq. (4), $\boldsymbol{Y}_{ij}$ is the δ-SPH diffusion term given by [31]:

$$\boldsymbol{Y}_{ij} = 2\left[(\rho_i - \rho_j)\frac{\boldsymbol{r}_{ij}}{|\boldsymbol{r}_i - \boldsymbol{r}_j|^2}\right]. \tag{6}$$

2.3 Model for surface dynamics

Surface dynamics, including surface tension, Marangoni force, and recoil pressure induced by evaporation, are fundamental components of melting pool dynamics. In this section, a novel scheme is proposed to estimate these surface forces, with a particular focus on calculating curvature and surface tangential temperature gradient. Additionally, the conventional SPH methods for modelling surface tension and Marangoni force are briefly reviewed.

2.3.1 Model for surface tension

Within the wider SPH research community, the continuum surface force (CSF) model proposed by Brackbill et al. [34] is widely used to simulate the surface tension and Marangoni force. Consequently, the normal and tangential surface forces are transformed into a volume force acting within a finite interface:

$$\boldsymbol{F}_s = \left(\underbrace{\sigma\kappa\boldsymbol{n}}_{surface\ tension} + \underbrace{\nabla_s\sigma}_{Marangoni\ force}\right)\delta_f, \tag{7}$$

where the σ is the surface tension coefficient (typically measured experimentally), κ is the surface curvature, $\boldsymbol{n}$ is the unit normal to the surface, ∇_s is the tangential surface gradient, δ_f is the surface delta function. The first term is the normal surface force (known as surface tension), while the second term is the tangential surface force (known as Marangoni force).

The surface normal and curvature are essential and sensitive parameters in the approximation of the surface tension force. In conventional SPH approaches, these variables are estimated with the following two steps:

3 Calculate the surface unit normal using the following equation as

$$\boldsymbol{n}_i = \frac{\nabla c_i}{|\nabla c_i|}\,, \tag{8}$$

in which the ∇c_i is obtained by:

$$\nabla c_i = \sum_j \frac{m_j}{\rho_j} \nabla_i W_{ij}\,. \tag{9}$$

4 Calculate the surface curvature as

$$\kappa_i = \sum_j (\boldsymbol{n}_j - \boldsymbol{n}_i) \cdot \nabla_i W_{ij} \frac{m_j}{\rho_j}\,. \tag{10}$$

However, it is argued that the above approach presents some limitations. First, the kernel gradient approximation in Eq. (10) could lose accuracy due to the truncated kernel support of the particles near the free surface. To address such issue, numerical corrections have been proposed and implemented in previous research reports [24, 25]. These include the kernel correction [24], and the kernel gradient correction [25]. In the kernel correction approach, Eq. (10) is modified as [24]:

$$\kappa_i = \frac{1}{\Gamma_i} \sum_j (\boldsymbol{n}_j - \boldsymbol{n}_i) \cdot \nabla_i W_{ij} \frac{m_j}{\rho_j}\,, \tag{11}$$

in which the correction factor Γ_i is obtained as:

$$\Gamma_i = \sum_j \frac{m_j}{\rho_j} W_{ij}\,. \tag{12}$$

While in the kernel gradient correction approach, Eq. (10) is modified as [25]:

$$\kappa_i = \sum_j (\boldsymbol{n}_j - \boldsymbol{n}_i) \cdot \widetilde{\nabla}_i W_{ij} \frac{m_j}{\rho_j}\,, \tag{13}$$

where the corrected kernel gradient $\widetilde{\nabla}_i W_{ij}$ is obtained by:

$$\widetilde{\nabla}_i W_{ij} = \mathbb{L}_i \nabla_i W_{ij}\,, \tag{14}$$

in which the corrected matrix $\mathbb{L}_i$ is obtained by [25]:

$$\mathbb{L}_i = \left(\sum_j (\boldsymbol{r}_j - \boldsymbol{r}_i) \otimes \nabla_i W_{ij} \frac{m_j}{\rho_j} \right)^{-1}. \tag{15}$$

In addition to correcting Eq. (10), the surface normal vector estimated by Eq. (8) is required to be filtered to further enhance the robustness of calculated curvature. Typically, the normal vector evaluated using Eqs. (8) and (9) could provide an accurate and robust approximation for particles near the free surface. However, for particles farther away from the free surface, the estimated normal vector could exhibit significant fluctuations due to the movement of neighbouring particles. Consequently, the estimated curvature and surface tension force could become unstable. To address this issue, the normal vectors incorporated in Eqs. (11) and (13) need to be filtered to select the reliable normals for the calculation of the curvature. One common approach to selecting the reliable normal vector is given as [4, 6, 8, 13, 24]:

$$\boldsymbol{n}_i = \begin{cases} \frac{\nabla c_i}{|\nabla c_i|} & if \quad |\nabla c_i| > \in \\ 0 & otherwise, \end{cases} \tag{16}$$

in which $\in$ is the designed cut-off value ($\in$= 0.01/h [24], $\in$= 0.1/h [4, 8, 13], $\in$= 0.2/h [6]). It should be noted that while increasing the cut-off value can enhance the consistency of the estimated curvature values, it may simultaneously reduce their accuracy.

Implementing the normal vector filter, the Eq. (11) can be written as [24]:

$$\kappa_i = \frac{1}{\Gamma_i^*} \sum_j (\boldsymbol{n}_j - \boldsymbol{n}_i) \cdot \nabla_i W_{ij} \frac{m_j}{\rho_j} \min(|\boldsymbol{n}_i|, |\boldsymbol{n}_j|)\,, \tag{17}$$

with a new kernel correction factor:

$$\Gamma_i^* = \sum_j \frac{m_j}{\rho_j} W_{ij} \min(|\boldsymbol{n}_i|, |\boldsymbol{n}_j|)\,. \tag{18}$$

The Eq. (13) can be written as [25]:

$$\kappa_i = \sum_j (\boldsymbol{n}_j - \boldsymbol{n}_i) \cdot \widetilde{\nabla}_i W_{ij} \frac{m_j}{\rho_j} \min(|\boldsymbol{n}_i|, |\boldsymbol{n}_j|)\,. \tag{19}$$

It should be noted that Eq. (16) is a basic and commonly used filter, while an enhanced filter can be found in [25]. In the conventional methods, such numerical corrections are essential to reduce errors and enhance the robustness of the SPH methodology deployed. However, some issues may still arise from implementing these corrections. For instance, when applying the kernel correction, Eq. (17)

was found to overestimate the surface tension force (see subsequent Sect. 3.1). It is acknowledged that implementing the kernel gradient correction could provide an accurate approximation for the surface tension force [25, 35]. Nevertheless, such correction and the associated intermediate calculations may increase the computational burden, as they involve the matrix inversion and minimum eigenvalue operations. Additionally, the kernel gradient correction may not be appropriate in the calculation of surface tangential temperature gradient due to the unified partition of smoothing kernel (see the subsequent Sect. 3.2).

For these reasons, a novel scheme for curvature calculation is proposed in this research. As shown in Fig. 1, the proposed scheme involves four steps:

(1) Detect the surface particles. In this step, two algorithms are employed. First, the possible surface particles are determined by the position divergence as:

$$\nabla \cdot \boldsymbol{r}_i = \sum_j (\boldsymbol{r}_j - \boldsymbol{r}_i) \cdot \nabla_i W_{ij} \frac{m_j}{\rho_j} . \tag{20}$$

Once $\nabla \cdot \boldsymbol{r}_i < 0.8 n_D$(where n_D is the dimension factor), a given particle i is determined to be a candidate surface particle. Then, all candidate surface particles are further investigated to determine whether they indeed belong to the real set of surface particles by using the algorithm presented in [36].

(2) Classify the neighbouring surface particles of a given surface particle into two categories. In this step, the surface tangential, $\boldsymbol{n}_i^\tau$, of a given surface particle i is first calculated as:

$$\boldsymbol{n}_i \cdot \boldsymbol{n}_i^\tau = 0 , \tag{21}$$

in which $\boldsymbol{n}_i$ is the surface normal vector calculated from Eq. (8). Then, the neighbouring surface particles j of a given surface particle i are classified into two categories as:

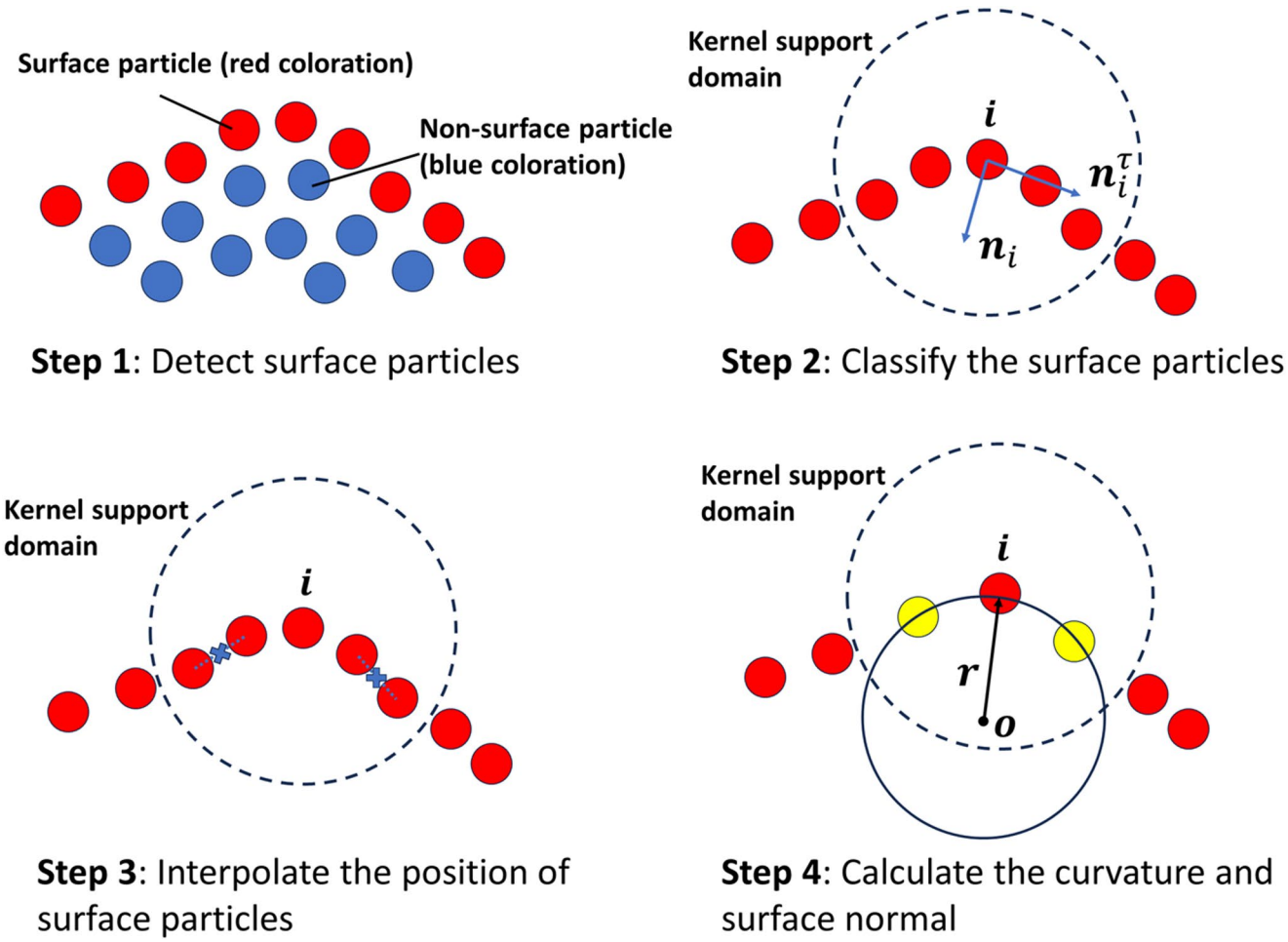

Fig. 1 The proposed scheme for the calculation of surface curvature and normal

$$j \in \begin{cases} \Gamma_1 & if \quad \boldsymbol{n}_i^{\tau} \cdot (\boldsymbol{r}_i - \boldsymbol{r}_j) > 0 \\ \Gamma_2 & otherwise. \end{cases} \tag{22}$$

(3) Interpolate the position of surface particles of each category. As a uniformed particle size is utilised in this study, the position of each particle in each category can be interpolated linearly as:

$$\begin{cases} \boldsymbol{r}_{j1} = \frac{1}{N_1} \sum_{j \in \Gamma_1} \boldsymbol{r}_j \ , \\ \boldsymbol{r}_{j2} = \frac{1}{N_2} \sum_{j \in \Gamma_2} \boldsymbol{r}_j \ , \end{cases} \tag{23}$$

in which N_1 and N_2 are the particle numbers of the group Γ_1 and Γ_2, respectively.

(4) Calculate the curvature and surface normal. In this step, the curvature and surface normal vector are calculated based on the position of particle i and its two neighbouring interpolated points (particles with yellow coloration presented in the step 4 of Fig. 1). As three points can define a unique circle, the curvature and surface normal can be obtained as:

$$\begin{cases} |\boldsymbol{r}_o - \boldsymbol{r}_i| = r \\ |\boldsymbol{r}_o - \boldsymbol{r}_{j1}| = r \\ |\boldsymbol{r}_o - \boldsymbol{r}_{j2}| = r \end{cases} , \ \kappa_i^* = \frac{1}{r} , \cdot \boldsymbol{n}_i^* = \frac{\boldsymbol{r}_o - \boldsymbol{r}_i}{|\boldsymbol{r}_o - \boldsymbol{r}_i|} , \tag{24}$$

where $\boldsymbol{r}_o$ is the position of the circle centre, r is the radius of the circle and κ_i^* and $\boldsymbol{n}_i^*$ are the surface curvature and normal vector of particle i, respectively.

Vergnaud et al. proposed a robust surface delta function, which was employed in this study [25]:

$$\delta_f = 2\, max(1,\ 0.5/\Gamma_i)\ |\nabla c_i| \ , \tag{25}$$

in which Γ_i and ∇c_i are calculated from Eqs. (12) and (9), respectively. Consequently, the body force of surface tension, $\boldsymbol{F}_{st}$, can be given by:

$$\boldsymbol{F}_{st} = \sigma_i \kappa_i^* \delta_f \, \boldsymbol{n}_i^* \ , \tag{26}$$

in which σ_i is the surface tension coefficient of particle i, κ_i^* and $\boldsymbol{n}_i^*$are the surface curvature and normal vector calculated from Eq. (24).

4.1 Model for Marangoni force

Typically, the surface tension coefficient is temperature dependent when a metallic material is in a molten state. Hence, it can be assumed that the surface tension coefficient is solely a function of temperature. Based on this assumption, the Marangoni force term presented in Eq. (7) can be expressed as follows [26]:

$$\boldsymbol{F}_{sm} = \frac{d\sigma_i}{dT_i} \left[\nabla_s T_i - (\nabla_s T_i \cdot \boldsymbol{n}_i^*)\, \boldsymbol{n}_i^*\right] \delta_f \ , \tag{27}$$

in which the surface temperature gradient $\nabla_s T_i$ is an essential variable of the above equation. Through SPH discretisation, the surface temperature gradient $\nabla_s T_i$ can be expressed as:

$$\nabla_s T_i = \sum_j (T_j - T_i) \nabla_i W_{ij} \frac{m_j}{\rho_j} \ . \tag{28}$$

It should be noted that $\nabla_s T_i$ has various SPH discrete forms, while Eq. (28) can lead to a reasonable approximation and small discretisation errors compared to other discrete forms [37]. Nevertheless, Eq. (28) could lose accuracy, particularly when particles have a truncated kernel support. Therefore, three different correction approaches for Eq. (28) have been employed in the previous research [4, 8, 13, 38]. First, Eq. (28) can be corrected using the kernel correction as [4, 8]:

$$\nabla_s T_i = \frac{1}{\Gamma_i} \sum_j (T_j - T_i) \nabla_i W_{ij} \frac{m_j}{\rho_j} \ , \tag{29}$$

in which the correction factor Γ_i is calculated from Eq. (12). Based on this approach, Lüthi et al. proposed an enhanced kernel correction form as [38]:

$$\nabla_s T_i = \frac{1}{\Gamma_i^{\#}} \sum_{j \in \mathbb{Z}_s} (T_j - T_i) \nabla_i W_{ij} \frac{m_j}{\rho_j} \ , \tag{30}$$

in which $\mathbb{Z}_s$ is the group of detected surface particles and $\Gamma_i^{\#}$ is the new correction factor given by:

$$\Gamma_i^{\#} = \sum_{j \in \mathbb{Z}_s} \frac{m_j}{\rho_j} W_{ij} \ . \tag{31}$$

In addition to these two corrections, the kernel gradient correction can be also employed [13]:

$$\nabla_s T_i = \sum_j (T_j - T_i) \widetilde{\nabla}_i W_{ij} \frac{m_j}{\rho_j} \ , \tag{32}$$

where the $\widetilde{\nabla}_i W$ is the corrected kernel gradient obtained from Eq. (14).

Although conventional correction approaches may improve Eq. (28) to some extent, each has its own limitations (see subsequent Sect. 3.2). Therefore, a novel approach is proposed in this study to estimate the surface temperature gradient. Since the neighbouring surface particles of a given particle i have been interpolated into two points, the surface temperature gradient can be directly obtained by:

$$\nabla_s T_i = 0.5 * \left(\frac{T_i - T_{j1}}{|\boldsymbol{r}_i - \boldsymbol{r}_{j1}|^2} \boldsymbol{r}_{ij1} + \frac{T_i - T_{j2}}{|\boldsymbol{r}_i - \boldsymbol{r}_{j2}|^2} \boldsymbol{r}_{ij2} \right) , \tag{33}$$

in which $\boldsymbol{r}_{ij1} = \boldsymbol{r}_i - \boldsymbol{r}_{j1}$, $\boldsymbol{r}_{ij2} = \boldsymbol{r}_i - \boldsymbol{r}_{j2}$, $\boldsymbol{r}_{j1}$ and $\boldsymbol{r}_{j2}$ are the position vector of the interpolated points from Eq. (23), T_{j1} and T_{j2} are the interpolated temperature obtained by:

$$\begin{cases} T_{j1} = \frac{1}{N_1} \sum\limits_{j \in F_1} T_j \ , \\ \\ T_{j2} = \frac{1}{N_2} \sum\limits_{j \in F_2} T_j \ . \end{cases} \tag{34}$$

In the subsequent Sect. 3.2, the calculated values of surface tangential temperature gradient obtained from the conventional approaches and the proposed method were compared using analytical solutions.

4.1.1 Model for recoil pressure

When a target is irradiated with a high power laser beam, solid material can undergo a phase change, leading to the formation of a melt pool. With the increase in laser power and irradiation time, the surface temperature of the molten material could also approach the boiling point, for which evaporation becomes more pronounced. Consequently, the recoil pressure induced by evaporation could play a significant role in melting pool dynamics during laser processing. The body force of recoil pressure $\boldsymbol{F}_r$ can be expressed as [5]:

$$\boldsymbol{F}_r = P_r \, \delta_f \, \boldsymbol{n}_r \, , \tag{35}$$

in which $\boldsymbol{n}_r$ is the unit normal vector pointing inward the material, δ_f is the surface delta function and P_r is the recoil pressure, which can be estimated from the saturated vapour pressure, P_{sat} [20]:

$$P_r = \left(\frac{1 + \beta_r}{2} \right) \cdot P_{sat} \, , \tag{36}$$

where $\beta_r = 0.17$ is the retro diffusion coefficient [20]. The saturated pressure can be obtained by the Clausius-Clapeyron equation:

$$P_{sat} = P_{atm} \exp \left[\frac{L_v M \left(T_i - T_b \right)}{R T_i T_b} \right] , \tag{37}$$

in which $P_{atm} = 1$atm is the atmospheric pressure, L_v is the latent heat of vaporisation, M is the molar mass, T_b is the boiling temperature and R is the ideal gas constant. In this study, the normal $\boldsymbol{n}_r$ presented in Eq. (35) is given by:

$$\boldsymbol{n}_r = \begin{cases} \boldsymbol{n}_i^* & if \ \ \kappa_i^* \neq 0 \ and \ \boldsymbol{n}_i \cdot \boldsymbol{n}_i^* > 0 \\ -\boldsymbol{n}_i^* & if \ \ \kappa_i^* \neq 0 \ and \ \boldsymbol{n}_i \cdot \boldsymbol{n}_i^* < 0 \\ \boldsymbol{n}_i & otherwise, \end{cases} \tag{38}$$

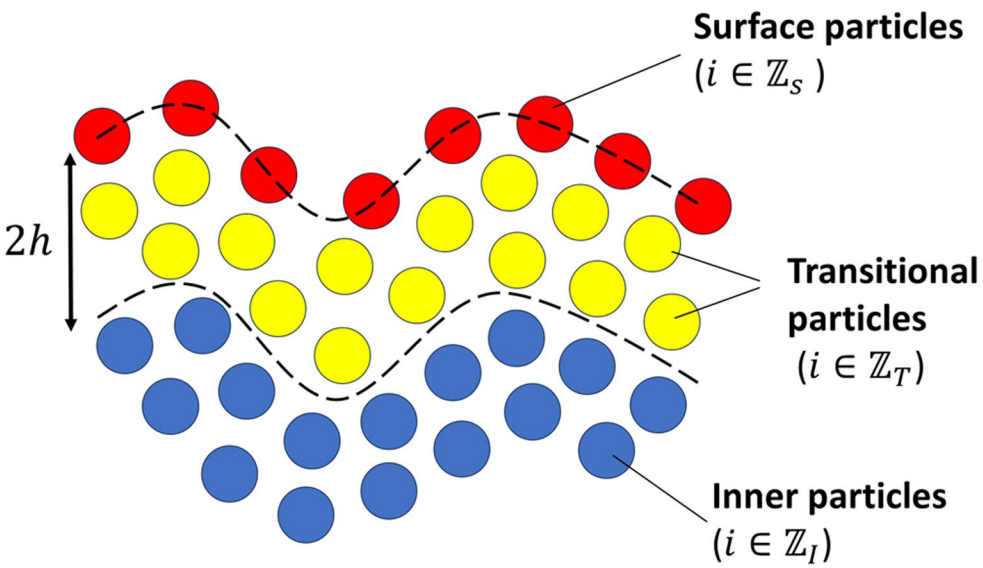

Fig. 2 Schematic of the particle set definition

Table 1 Numerical setup and parameters used in the test case of droplet deformation

Property	Value
Density (ρ)	1000 kg/m^3
Viscosity (μ)	0.1 kg/(m s)
Surface tension coefficient (σ)	0.05 N/m
Initial computational domain ($L \times L$)	10×10 mm^2
Particle size	0.25 mm
Total number of particles	1,681

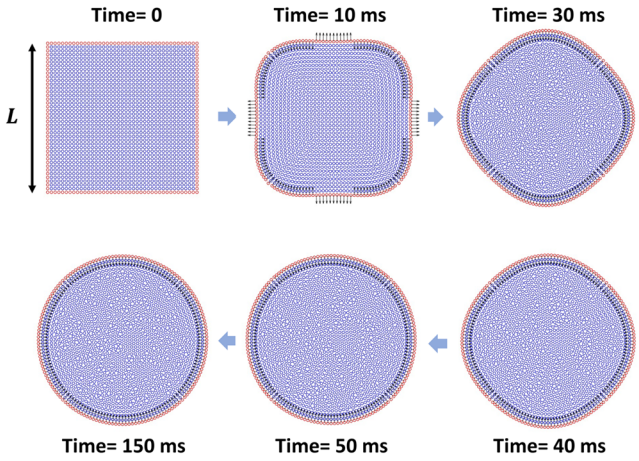

Fig. 3 Simulated evolution of an initial square droplet onto a circular shape under the effects of surface tension

where the $\boldsymbol{n}_i$ is the normal calculated from Eq. (8), while $\boldsymbol{n}_i^*$ is obtained from Eq. (24).

4.2 Computational model for heat transfer and laser absorption

The differential equation governing the heat transfer problem between the incident laser beam and the irradiated material is expressed as:

$$c_p \frac{dT}{dt} = \frac{1}{\rho} \nabla \cdot (k \nabla T) + Q_{laser} - Q_{loss} \,, \tag{39}$$

where c_p is the specific heat capacity, ρ is the density, k is the thermal conductivity, Q_{laser} is the laser source, and Q_{loss} is the heat loss. The heat conduction term, $\frac{1}{\rho} \nabla \cdot (k \nabla T)$, can be written in a SPH discrete form [39]. Consequently, Eq. (39) can be expressed as:

$$c_{p,i} m_i \frac{dT_i}{dt} = \sum_j \frac{m_i m_j}{\rho_i \rho_j} \left(\frac{4 k_i k_j}{k_i + k_j} \right) \left(\frac{T_i - T_j}{|\boldsymbol{r}_i - \boldsymbol{r}_j|^2} \right) \boldsymbol{r}_{ij} \cdot \nabla_i W_{ij} + Q_{laser} - Q_{loss} \,, \tag{40}$$

where $c_{p,i}$ is the specific heat capacity of particle i, k_i and k_j are the thermal conductivity of particle j and particle i, respectively. In this study, the laser intensity profile was approximated to follow a Gaussian profile. Therefore, the laser source term can be expressed as [20]:

$$Q_{laser} = \alpha \, A_g \frac{E_p}{\tau_p \pi \, r_b^2} \exp\left(\frac{-2x^2}{r_b^2} \right) \,, \tag{41}$$

where α is energy absorption coefficient, A_g is the top surface area of a grid cell in the implemented grid-based laser absorption scheme (the detailed procedure of this scheme can be found in [16]), E_p is the pulse energy, τ_p is the pulse duration and r_b is the radius of laser beam. The heat loss due to convection, radiation and evaporation was considered in this study as:

$$Q_{loss} = A_p [h_c (T_s - T_0) + \epsilon \, \sigma_B (T_s^4 - T_0^4) + L_v \dot{m}] \,, \tag{42}$$

in which A_p is the top surface area of a SPH particle (approximated to V_0/dx, where V_0 is the initial volume of particle and dx is the particle size), T_s is the surface temperature, T_0 is the ambient temperature (assumed to be 300 K), h_c is the convection factor, ϵ is the emissivity, σ_B is the Stefan–Boltzmann constant, L_v is the latent heat of vaporisation and $\dot{m}$ is the surface mass flow rate due to evaporation, estimated by the Hertz-Knudsen equation [20, 40] as:

$$\dot{m} = (1 - \beta_r) \sqrt{\frac{m_a}{2\pi \, k_b T_s}} P_{sat} \,, \tag{43}$$

where β_r is the retro diffusion coefficient [20], m_a is the atomic mass, k_b is the Boltzmann constant, P_{sat} is saturated vapour pressure.

4.3 Time integration scheme

In this study, the predictor-corrector time integration scheme presented in [41] is employed. In this scheme, the values of the field variables are calculated at the half time-step by the predictor step as:

$$\begin{cases} \boldsymbol{u}_i^{n+\frac{1}{2}} = \boldsymbol{u}_i^n + \frac{\Delta t}{2} \boldsymbol{F}_i^n \,; \; \rho_i^{n+\frac{1}{2}} = \rho_i^n + \frac{\Delta t}{2} D_i^n \,; \\ \boldsymbol{r}_i^{n+\frac{1}{2}} = \boldsymbol{r}_i^n + \frac{\Delta t}{2} \boldsymbol{u}_i^n \,; \; p_i^{n+\frac{1}{2}} = f\left(\rho_i^{n+\frac{1}{2}}\right) \,; \\ T_i^{n+1/2} = T_i^n + \frac{\Delta t}{2} H_i^n \,, \end{cases} \tag{44}$$

where the current time-step is denoted by the superscript n. Then, these variables are corrected at the half time-step by the corrector step as:

$$\begin{cases} \boldsymbol{u}_i^{n+\frac{1}{2}} = \boldsymbol{u}_i^n + \frac{\Delta t}{2} \boldsymbol{F}_i^{n+\frac{1}{2}} \,; \; \rho_i^{n+\frac{1}{2}} = \rho_i^n + \frac{\Delta t}{2} D_i^{n+\frac{1}{2}} \,; \\ \boldsymbol{r}_i^{n+1/2} = \boldsymbol{r}_i^n + \frac{\Delta t}{2} \boldsymbol{u}_i^{n+1/2} \,; \; T_i^{n+1/2} = T_i^n + \frac{\Delta t}{2} H_i^{n+1/2} \,. \end{cases} \tag{45}$$

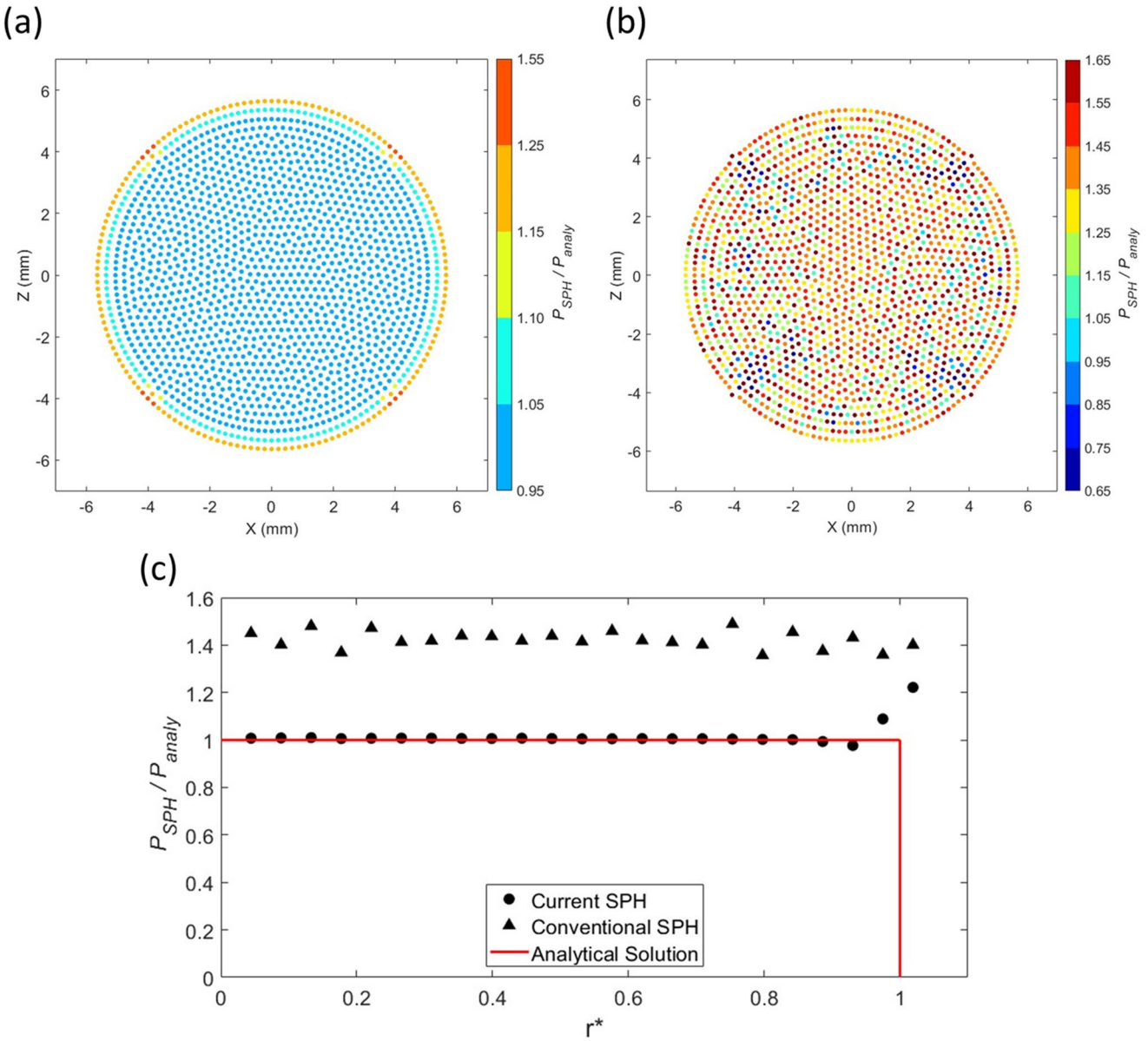

Fig. 4 **a** Particle position and corresponding pressure distribution at t =150 ms obtained from the proposed approach; **b** Particle position and corresponding pressure distribution at t =150 ms obtained from the conventional method; **c** Pressure profiles from the centre of droplet to the boundary at t =150 ms

Finally, these values are calculated at the next time step by the equation below:

$$\begin{cases} \boldsymbol{u}_i^{n+1} = 2\boldsymbol{u}_i^{n+\frac{1}{2}} - \boldsymbol{u}_i^n \; ; \; \rho_i^{n+1} = 2\rho_i^{n+\frac{1}{2}} - \rho_i^n \; ; \\ p_i^{n+1} = f\left(\rho_i^{n+1}\right) \; ; \; T_i^{n+1} = 2T_i^{n+1/2} - T_i^n \; . \end{cases} \tag{46}$$

Given that the particle shifting technique was applied outside the sub-time-steps of time integration, the particle position at the next time step was updated as:

$$\boldsymbol{r}_i^{n+1} = 2\boldsymbol{r}_i^{n+1/2} - \boldsymbol{r}_i^n + \delta\, \boldsymbol{r}_i^{n+1/2} \; . \tag{47}$$

To ensure numerical stability, the CFL conditions employed in [38] were utilised to compute the momentum, surface tension, viscosity, and heat diffusion by the respective conditions expressed in the equation below:

$$\Delta t \leq \min\left(0.25\frac{h}{c_0},\, 0.25\sqrt{\frac{\rho\, h^3}{2\pi\, \sigma}},\, 0.125\frac{\rho\, h^2}{\mu},\, 0.125\frac{\rho\, c_p h^2}{k}\right) . \tag{48}$$

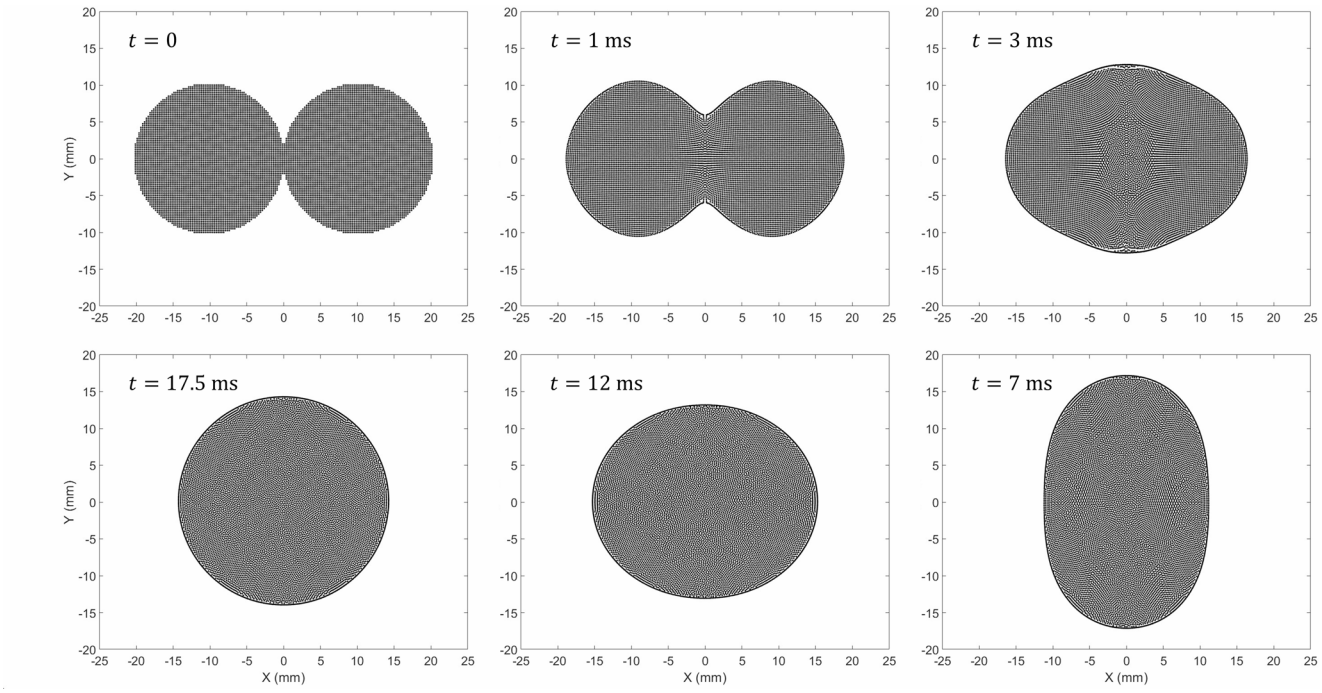

Fig. 5 Simulated collision of two circular droplets and formation of a single droplet under the effects of surface tension

Table 2 Numerical setup and parameters used in the test case of droplets collision

Property	Value
Density (ρ)	1 kg/m^3
Viscosity (μ)	0.005 kg/(m s)
Surface tension coefficient (σ)	0.1 N/m
Initial radius of each droplet (r_0)	10 mm
Particle size	0.25 mm
Total number of particles	10,434

4.4 Additional numerical procedures

To further enhance the robustness and accuracy of the developed SPH framework, additional numerical treatments were incorporated in the conducted simulations, including the XSPH correction [42], tensile correction [43], enhanced particle shifting technique, barrier forces and the velocity damping of phase transformation. As the XSPH correction and tensile correction have been widely utilised in numerous SPH models, they are not presented in this paper. The detailed procedure of these corrections can be found in [42, 43]. Instead, the remainder of this section presents the enhanced particle shifting technique, barrier forces and velocity damping of phase transformation.

4.4.1 Enhanced particle shifting technique

Due to the small gradient of kernel, SPH particles may clump together when close to each other [35]. Consequently, error and numerical instability resulting from particle clumping could emerge in the simulations. To address this issue, the particle shifting technique (PST) based on Fick's law of diffusion was developed, which can be expressed as [32, 35]:

$$\delta \boldsymbol{r}_i = -\alpha_s h^2 \sum_j (1+\chi_i) \nabla_i W_{ij} \frac{m_j}{\rho_j} \text{ with } \chi_i = 0.2\left[\frac{W_{ij}}{W(dx)}\right]^4, \tag{49}$$

in which α_s is a case-dependent coefficient, h is the smoothing length and χ_i is the artificial pressure-like function, which could prevent pairing instability [32]. However, the particle shifting technique can introduce additional errors for the particles near the free surface due to their truncated kernel support. In particular, the sub-surface particles could be shifted toward the free surface, resulting an un-physical surface expansion. To mitigate the additional errors raised from PST, a free surface correction factor ψ was incorporated in Eq. (49) as follows:

$$\delta \boldsymbol{r}_i = -\psi_i \alpha_s h^2 \sum_j (1+\chi_i) \nabla_i W_{ij} \frac{m_j}{\rho_j}. \tag{50}$$

Inspired by the work of Sun et al. [44–46], the value of ψ_i depends on the region where a particle belongs and is given by:

$$\psi_i = \begin{cases} 0 & \text{if particle } i \in \text{surface particles } (\mathbb{Z}_s) \\ \xi_i \ (\mathbb{I} - \boldsymbol{n}_i^s \otimes \boldsymbol{n}_i^s) & \text{if particle } i \in \text{transitional particles } (\mathbb{Z}_T) \\ 1 & \text{if particle } i \in \text{inner particles } (\mathbb{Z}_I) \end{cases}, \tag{51}$$

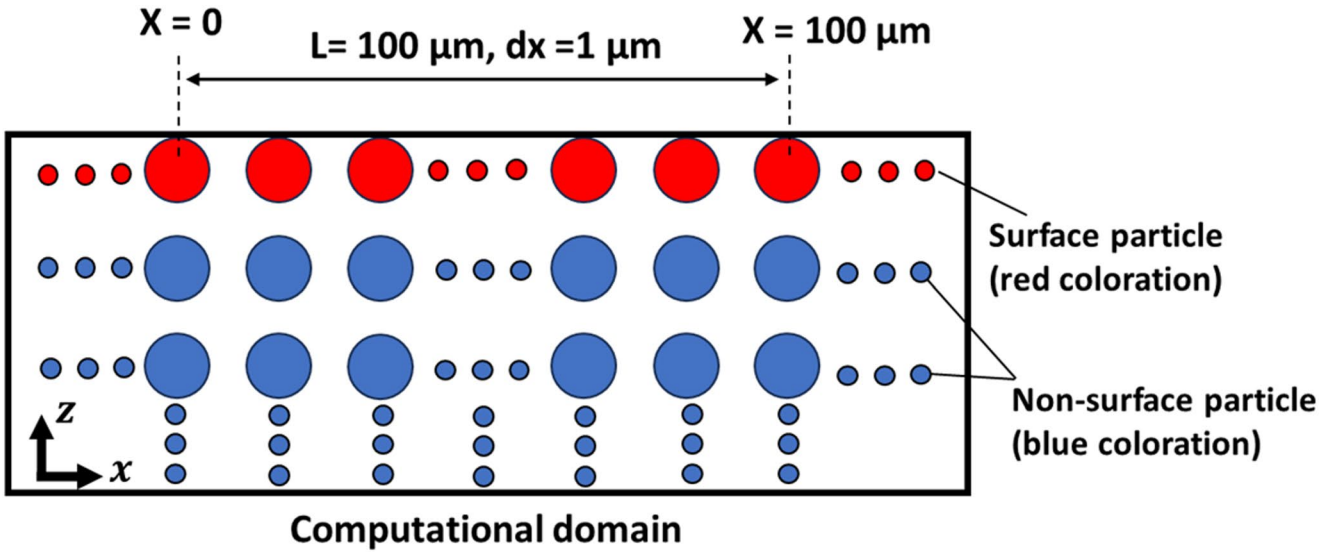

Fig. 6 Schematic of the computational domain designed to evaluate the approximation error of surface tangential temperature gradient

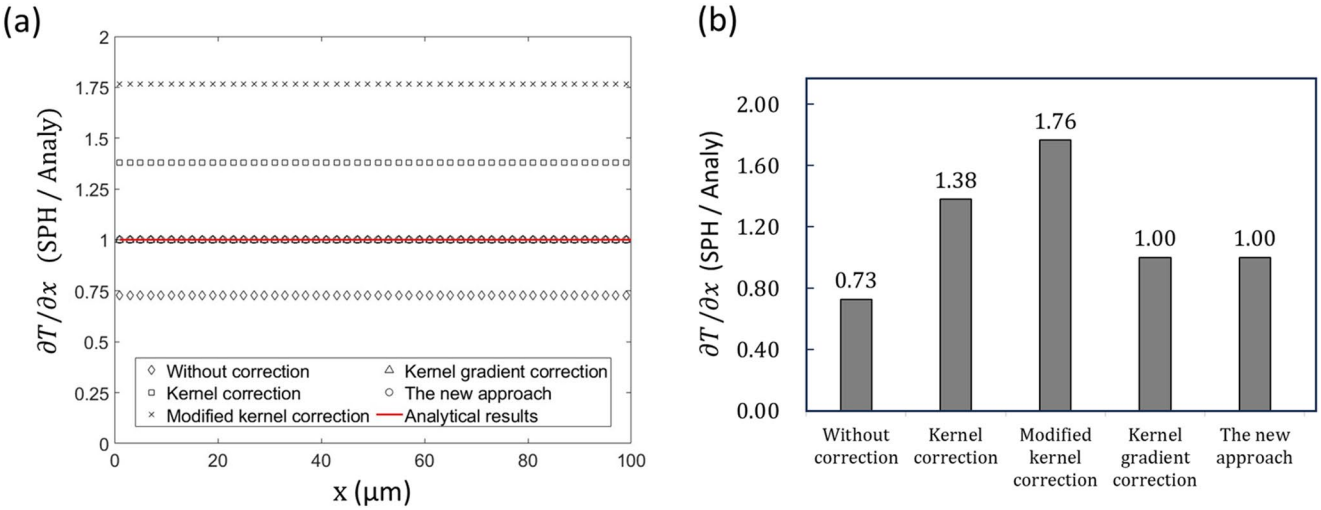

Fig. 7 **a** Estimated surface tangential temperature gradients as a function of position in a computational domain with a linear temperature distribution; **b** Average ratios of the surface tangential temperature gradient obtained by different approaches in a computational domain with a linear temperature distribution

where ξ_i is the designed smoothing factor, $\mathbb{I}$ is the identity tensor, and $\boldsymbol{n}_i^s$ is the unit vector perpendicular to the free surface. Figure 2 shows schematic of the defined three regions, in which the particles with red, yellow and blue coloration are the surface particles, transitional particles and inner particles, respectively. The value of $\boldsymbol{n}_i^s$ could be estimated using the kernel gradient approximation method, such as Eq. (8) and its corrected form presented in [44]. Nevertheless, such approach may introduce errors when particles exhibit an irregular distribution. To improve the robustness, $\boldsymbol{n}_i^s$ in this study is approximated by:

$$\boldsymbol{n}_i^s = \frac{\boldsymbol{r}_i^f}{\left|\boldsymbol{r}_i^f\right|} \quad \text{with} \quad \boldsymbol{r}_i^f = \sum_{i\in\mathbb{Z}_T, j\in\mathbb{Z}_s} \frac{\boldsymbol{r}_{ij}}{\left|\boldsymbol{r}_{ij}\right|^3}, \tag{52}$$

in addition, the designed smoothing factor ξ_i is given by:

$$\xi_i = \frac{1}{1+\alpha_1 \eta_i^{\alpha_2}} \quad \text{with} \quad \eta_i = \sum_{j\in\mathbb{Z}_s} (\boldsymbol{r}_j - \boldsymbol{r}_i)\cdot\nabla_i W_{ij}\frac{m_j}{\rho_j}, \tag{53}$$

in which α_1 and α_2 are positive constants to control the smoothing effects. When the transitional particles approach the free surface, the magnitude of PST distance is expected to be reduced by applying the smoothing factor

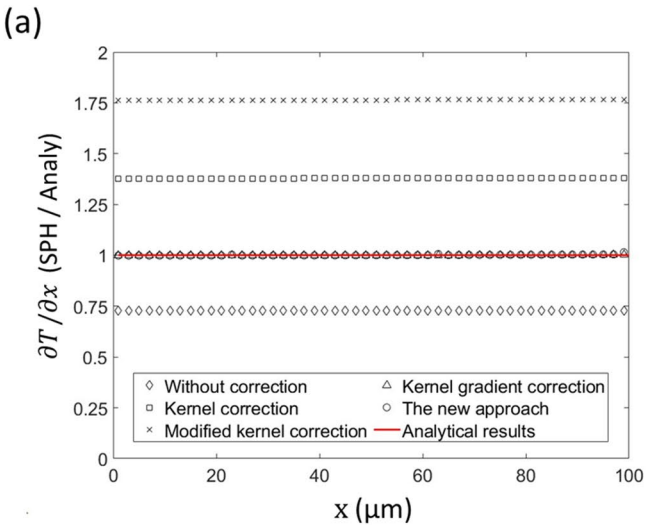

Fig. 8 **a** Estimated surface tangential temperature gradients as a function of position in a computational domain with a Gaussian temperature distribution; **b** Average ratios of the surface tangential temperature gradient obtained by different approaches in a computational domain with a Gaussian temperature distribution

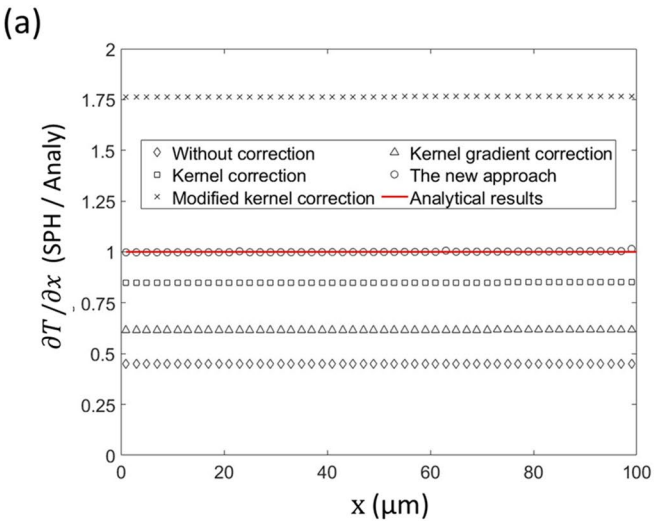

Fig. 9 **a** Estimated surface tangential temperature gradients as a function of position in a computational domain with a temperature distribution described in Eq. (63); **b** Average ratios of the surface tangential temperature gradient obtained by different approaches in a computational domain with a temperature distribution described in Eq. (63)

ξ_i. Therefore, the free surface error induced by PST can be further mitigated.

4.4.2 Barrier forces and velocity damping

An irregular distribution of particles can lead to numerical instabilities and errors in the simulations. To further maintain a reasonable particle distribution, the additional elastic and viscous barrier forces proposed in [9] were incorporated into the developed SPH model. These barrier forces are defined as:

$$\boldsymbol{F}_b^i = \sum_j (D_b k_e + D_b k_v \Pi_{ij}) \frac{\boldsymbol{r}_{ij}}{|\boldsymbol{r}_{ij}|}, \tag{54}$$

in which k_e and k_v are the stiffness and damping constant and D_b and Π_{ij} are given by:

$$D_b = \begin{cases} \frac{r_b^* - |\boldsymbol{r}_{ij}|}{h} & if \quad |\boldsymbol{r}_{ij}| < r_b^* \\ 0 & otherwise \end{cases}, \Pi_{ij} = -\frac{\boldsymbol{v}_{ij} \cdot \boldsymbol{r}_{ij}}{|\boldsymbol{r}_{ij}|}, \tag{55}$$

where r_b^* is the threshold to activate the barrier forces. Its value was set as $r_b^* = 0.9dx$(where dx is the particle size) in this study. Due to the low value of the set threshold, the

incorporated barrier forces are only activated in rare scenarios, therefore, have no significant influence on the simulated flow.

In this study, when the temperature of particles is below the solidus temperature, they are assumed to be fixed in space. Furthermore, when their temperature is within the temperature band of phase transformation, a velocity damping term is introduced as:

$$\boldsymbol{v}_i = \frac{\boldsymbol{v}_i}{1+\epsilon_d} \quad \text{if} \quad T_s^* \leq T_i \leq T_l^* \,, \tag{56}$$

where ϵ_d is the velocity damping factor, set to 0.025 [47], T_s^* and T_l^* are the solidus and liquidus temperatures, respectively.

5 Initial numerical verification of surface tension and Marangoni force

As surface tension and Marangoni force are essential components of melting pool dynamics, test cases were conducted to verify the accuracy of the proposed surface tension model and Marangoni model. In particular, results obtained from applying conventional approaches and the proposed scheme are presented and discussed. In this study, all simulations were implemented by modifying the 2D parallel open-source code 'parallelSPHysics' [48]. Furthermore, the Cubic-Spline kernel function [49] with a smoothing length $h = 1.5\,dx$ was utilised in the simulations.

5.1 Verification of the developed surface tension model

5.1.1 Droplet deformation

A square liquid droplet driven by the surface tension force was first investigated. Under the effects of the surface tension force, the droplet can exhibit a transformation from the initial square shape to a circular shape. In addition, it should be noted that gravity was neglected in this test case. When the system reaches an equilibrium state, the analytical pressure at the steady state can be obtained by [35]:

$$P_{analy} = \frac{\sigma}{R_{eq}} \quad \text{with} \quad R_{eq} = \frac{L}{\sqrt{\pi}} \,, \tag{57}$$

in which σ is the surface tension coefficient, R_{eq} is the radius of the final droplet, and L is the length of initial droplet. The numerical setup and parameters utilised in the simulations are presented in Table 1.

Figure 3 shows the simulated evolution of a square droplet into a circular droplet with the effects of surface tension. It should be noted the particles with red colouration are the detected surface particles using the surface detection scheme presented in Sect. 2.2.1. In addition, the arrows presented in the figure are the surface normals obtained from Eq. (24). It can be said that the considered surface detection scheme and the proposed surface normal calculation approach have provided reasonable outcomes.

Figure 4a shows the pressure distribution at $t = 150$ ms(corresponding to the last sub-figure of Fig. 3) using the proposed method. It can be observed that the simulated pressure using the approach proposed in this research displays a good agreement with the analytical results. It is noted that the

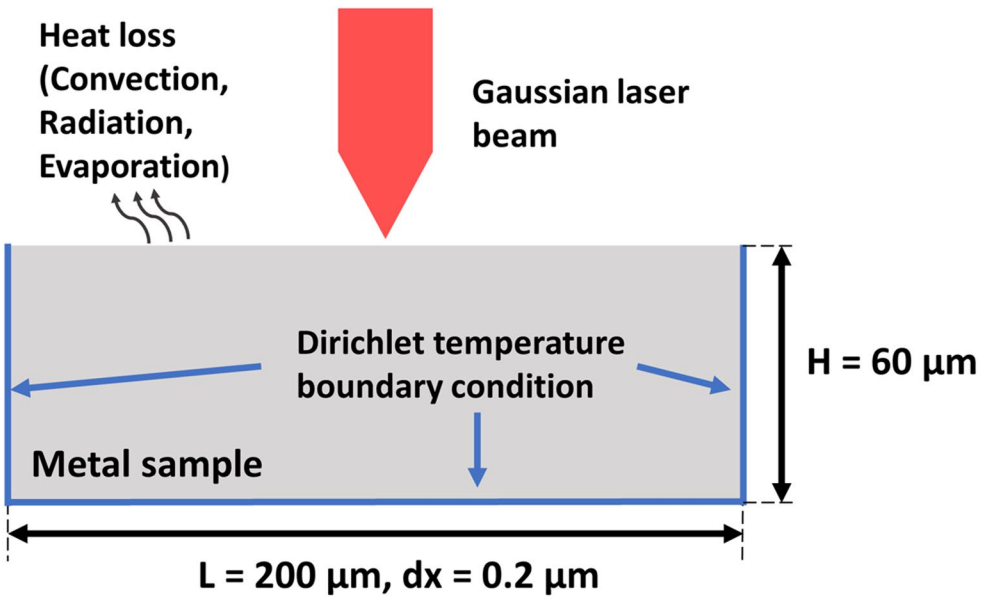

Fig. 10 The computational domain of the SPH model of laser micro texturing and related model setups

Table 3 Material parameters and laser parameters used in the simulation of laser micro texturing [20, 27, 51, 52]

Parameter	Temperature	Value	Units
Melting temperature (T_m)		1923	K
Temperature band of phase transformation ($\delta\, T$)		200	K
Liquidus temperature (T_l^*)		$T_m + \frac{\delta\, T}{2}$	K
Solidus temperature (T_s^*)		$T_m - \frac{\delta\, T}{2}$	K
Boiling temperature (T_b)		3533	K
Latent heat of fusion (L_m)		$2.86 \times\ 10^5$	J/kg
Latent heat of evaporation (L_v)		9.83×10^6	J/kg
Emissivity (ϵ)		0.45	-
Convection factor (h_c)		20	W/(m^2 K)
Density (ρ)	$T \leq\ T_s^*$	4420	Kg/m^3
	$T_s^* < T < T_l^*$	$4420 - \frac{500\ (T - T_s^*)}{\delta\, T}$	
	$T \geq\ T_l^*$	3920	
Thermal conductivity (k)	$T < 1268$	$1.260 + 0.016T$	W/(m K)
	$1268 \leq\ T \leq\ T_m$	$3.513 + 0.013T$	
	$T > T_m$	$-12.752 + 0.024T$	
Specific heat capacity (c_p)	$T \leq\ 1268$	$483.04 + 0.22T$	J/(kg K)
	$1268 < T < T_s^*$	$412.70 + 0.18T$	
	$T_s^* \leq\ T \leq\ T_l^*$	$\frac{(412.70 + 0.18T_s^*) + 831}{2} + \frac{L_m}{\delta\, T}$	
	$T > T_l^*$	831.0	
Viscosity (μ)	$T \leq\ T_s^*$	0.05	Kg/(m s)
	$T_s^* < T < T_l^*$	$0.05 - 0.045 * \frac{(T - T_s^*)}{\delta\, T}$	
	$T \geq\ T_l^*$	0.005	
Surface tension coefficient (σ)	$T > T_s^*$	$1.0 - 0.28 \times\ 10^{-3}\ (T - T_s^*)$	N/m
Marangoni coefficient ($d\sigma\ /dT$)		$0.28 \times\ 10^{-3}$	N/(m· K)
Pulse duration ($\tau\ _p$)		8.6	µs
Pulse energy (E_p)		1.574	mJ
Beam radius (r_b)		52.8	µm
Energy absorption coefficient (α)		0.6	-

specific pressure value at the boundary presents a relatively large deviation from the analytical results. This deviation is likely to be a common issue in single-phase simulations, as the particles near the boundary have a truncated kernel support. Such difference can also be observed in the case tests conducted in [5, 25, 35]. Although the deviation exists at the boundary, the average pressure error estimated by:

$$error = \frac{\sum\ |P_i - P_{analy}|}{N \cdot\ P_{analy}}\ , \tag{58}$$

was found to be less than 4%. In the above Eq. (58), N is the particle number of computational domain. For comparison, Fig. 4b shows simulation results at t =150 ms, for which the curvature was estimated using the conventional method, i.e., Eq. (17). It can be found the simulated pressure field obtained from the conventional approach presents a large deviation compared to the analytical solution. To further visualise the obtained results, the pressure values at t =150 ms from the centre of droplet to the boundary are shown in Fig. 4c. In particular, pressure values are plotted against the non-dimensional distance, in which the value of radial axis r^* is obtained by:

$$r^* = \frac{|r_i - r_o^*|}{R_{eq}} \quad \text{with} \quad r_o^* = \frac{\sum\ r_i}{N}\ . \tag{59}$$

Through these comparisons, it can be said the proposed scheme for modelling surface tension could be more accurate than the conventional method. In addition to the conventional method, Vergnaud et al. [25] recently proposed a robust C-CSF scheme to model the surface tension force. As the C-CSF scheme has been successfully employed in this test case [5, 25, 35], it could also be a good alternative

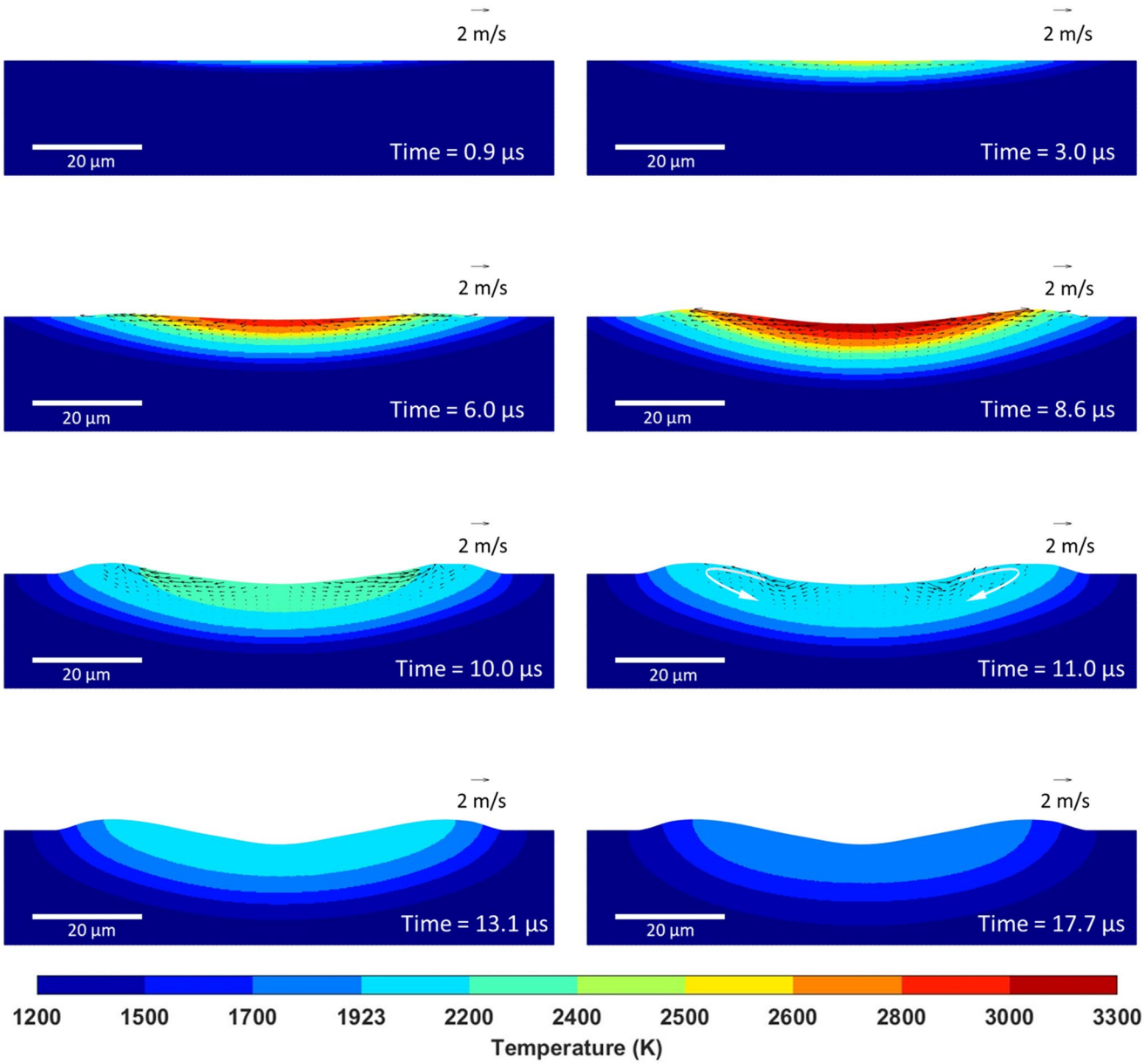

Fig. 11 Snapshots of the SPH simulated evolution in time of laser micro texturing for a pulse duration of 8.6 µs irradiating a Ti6Al4V target with a deliver pulse energy of 1.574 mJ

method to model the surface tension force. Nevertheless, it should be noted the proposed scheme not only accurately models surface tension but is also adaptable for simulating the Marangoni force, as will be shown in Sect. 3.2. Considering this, it is argued that the proposed scheme still holds its unique advantages.

5.1.2 Droplet collision

Following the successful implementation of the first test case, an additional test case was conducted to further establish the robustness and accuracy of proposed scheme for modelling surface tension. The initial computational domain generated for this test case is illustrated at $t = 0$ of Fig. 5, in which two circular droplets collide with an initial velocity of:

$$\boldsymbol{v}_0 = \quad U_0 \frac{x_i}{r_0}\,, \tag{60}$$

where $U_0 = 1$ m/s, r_0 is the initial radius of the two droplets. The numerical setup and parameters utilised in this simulation are presented in Table 2. Again, the gravity was neglected in this test case.

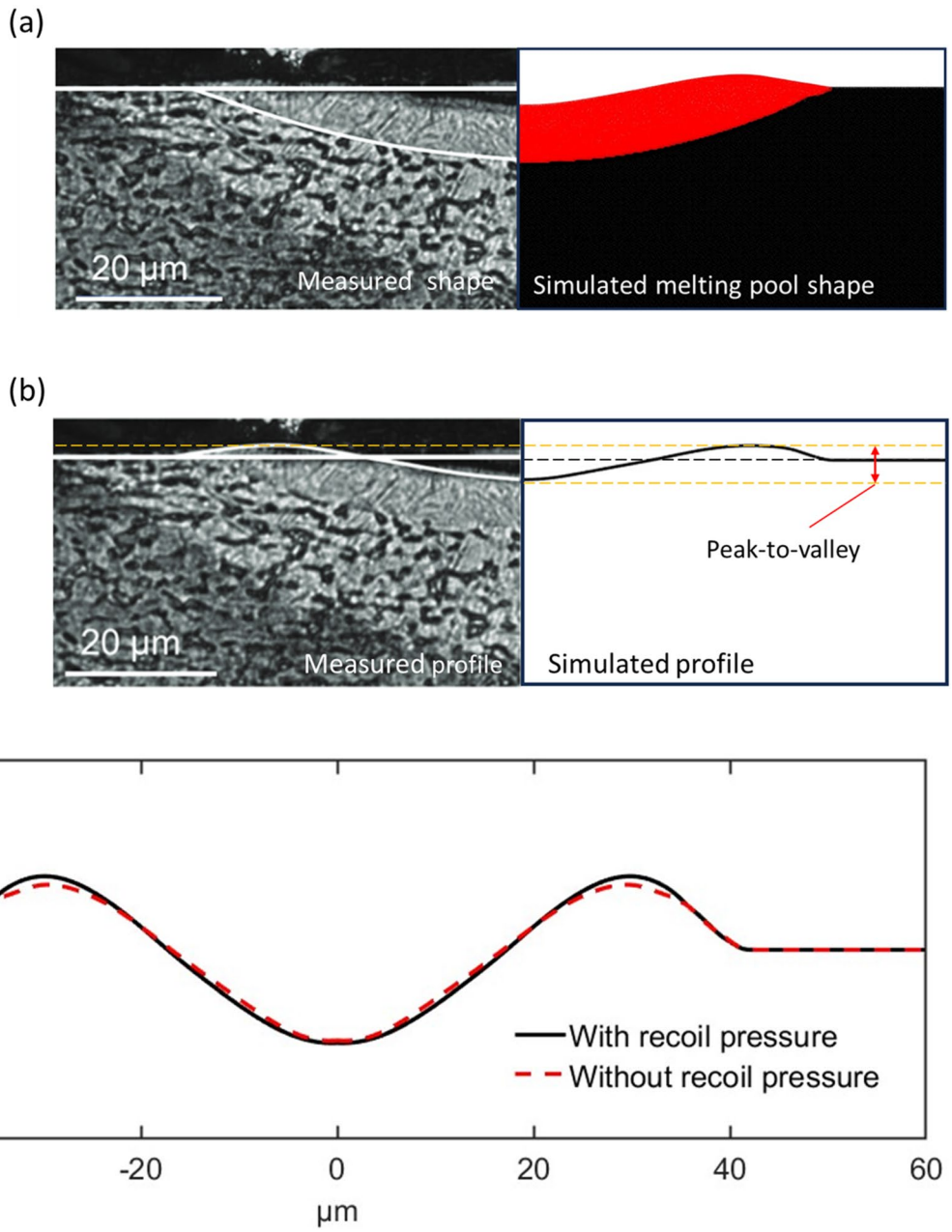

Fig. 12 Comparison between simulated and experimental results: **a** melt pool shape; **b** solidified surface profile. The experimental micrographs are reprinted from Ma et al. [28] Copyright (2025), with permission from ASME under License number 1613323-1

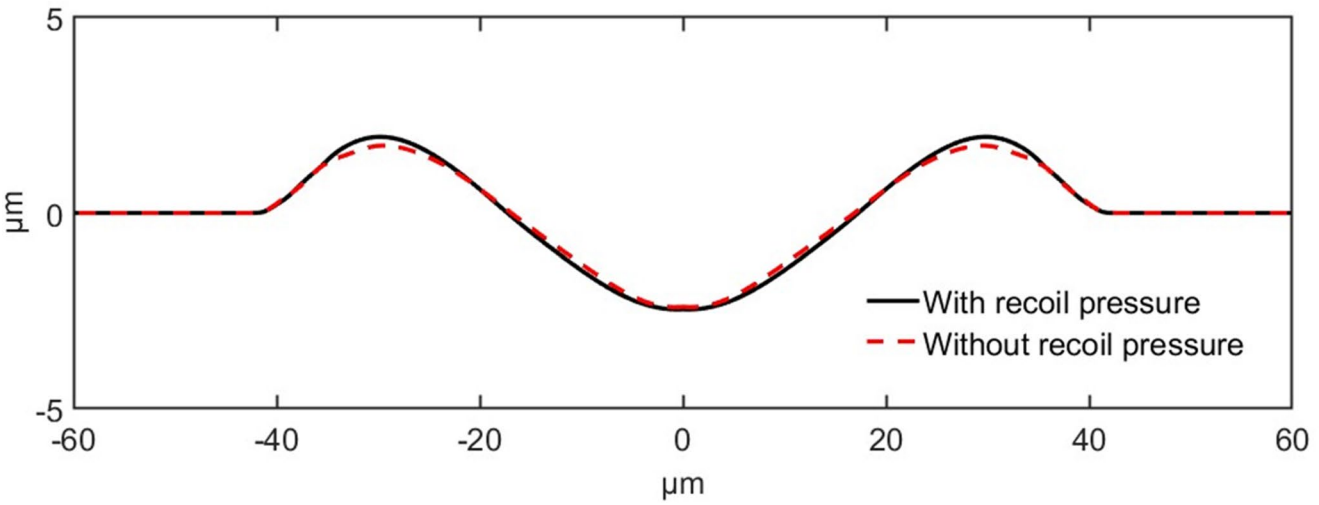

Fig. 13 Simulated solidified surface profiles with and without the inclusion of recoil pressure

Figure 5 shows the progression of collision of two circular droplets with the initial velocity described in Eq. (60). It can be observed that the droplets merge into a single larger droplet due to the effects of surface tension. Furthermore, the combined droplet undergoes periodical oscillations before reaching an equilibrium state at around $t = 30$ ms. The simulated radius of the combined droplet at the steady state is 14.18 mm, which closely aligns with the analytical result of 14.14 mm.

5.2 Verification of the proposed scheme for modelling Marangoni force

As mentioned in Sect. 2.2.2, the Marangoni force can be approximated as a function of surface tangential temperature gradient. Consequently, accurately estimating the temperature gradient is essential. In this section, numerical tests were conducted to evaluate the errors in the calculated surface tangential temperature gradients obtained from the conventional approaches and the proposed method. To facilitate the straightforward derivation of corresponding analytical

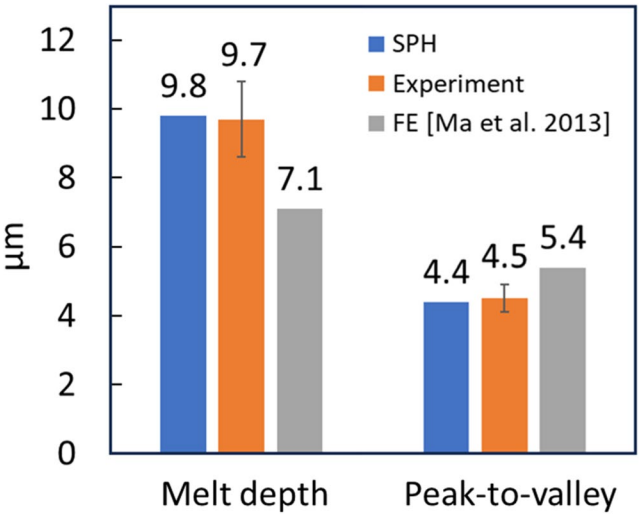

Fig. 14 Comparison of simulated results from the SPH model and the FE model from [27]

solutions, a rectangle computational domain was generated, in which all particles were fixed in space and uniformly distributed. Temperature gradients were initially set within the computational domain before outputting the estimated tangential temperature gradients at the surface from $x = 0$ to $x =$100 μm. The schematic of the generated computational domain for this case test is shown in Fig. 6. It is important to note that the temperature of particles was assumed to remain constant after the initialisation of the temperature gradients.

Test 1: The computational domain is assumed to follow a linear temperature distribution given by:

$$T_i = k_t x + B_t \,, \tag{61}$$

in which $k_t = -20/dx$, $B_t = 3000$. As shown in Fig. 7a, the estimated surface tangential temperature gradients obtained from the conventional approaches and proposed method were plotted as a function of position. In particular, the temperature gradients labelled as 'Without correction', 'Kernel correction', 'Modified kernel correction', 'Kernel gradient correction' and 'The new approach' were obtained from Eqs. (28), (29), (30), (32) and (33), respectively. Figure 7b shows the average ratios of the surface tangential temperature gradients obtained from different approaches. It can be noted the kernel gradient correction and the proposed new approach can provide an accurate approximation in this test case, while the other approaches present a relatively larger deviation from the analytical results.

Test 2: Given that some lasers exhibit a Gaussian intensity profile, the computational domain for this second test case is now assumed to follow a Gaussian temperature distribution as:

$$T_i = A_t \exp\left(\frac{-x^2}{r_t^2}\right) + B_t^* \,, \tag{62}$$

in which $A_t = 3000$, $B_t^* = 300$ and $r_t = 50$ μm. Figure 8 shows the estimated surface tangential temperature gradients and their average ratios obtained by different approaches. Again, the results derived from kernel gradient correction and the proposed new approach are in a good agreement with the analytical results.

Test 3: When the target is irradiated by lasers with high intensity, the surface temperature gradient may significantly differ from that of the sub-surface. This scenario can be commonly observed in laser manufacturing, such as laser ablation and laser powder bed fusion. To account for this factor, the temperature distribution in this test case was assumed as:

$$T_i = \begin{cases} A_t \exp\left(\frac{-x^2}{r_t^2}\right) + B_t^* & if\ particle\ i \in\ surface\ particle \\ B_t^* & otherwise, \end{cases} \tag{63}$$

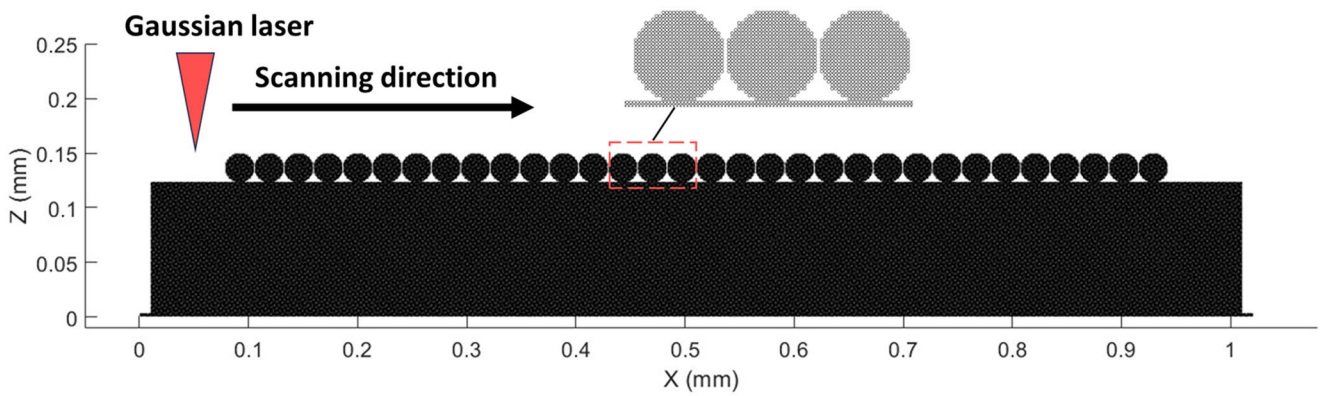

Fig. 15 The computational domain of the SPH model of laser powder bed fusion

Table 4 Material parameters used in the simulations of laser powder bed fusion [4, 5, 53]

Parameter	Temperature	Value	Units
Melting temperature (T_m)		1723	K
Temperature band of phase transformation ($\delta\, T$)		100	K
Liquidus temperature (T_l^*)		$T_m + \frac{\delta\, T}{2}$	K
Solidus temperature (T_s^*)		$T_m - \frac{\delta\, T}{2}$	K
Boiling temperature (T_b)		3100	K
Latent heat of fusion (L_m)		$2.47 \times\ 10^5$	J/kg
Latent heat of evaporation (L_v)		6.36×10^6	J/kg
Emissivity (ϵ)		0.40	-
Convection factor (h_c)		50	W/(m^2 K)
Density (ρ)		7500	Kg/m^3
Thermal conductivity (k)	$T \leq\ T_m$	20.93	W/(m K)
	$T > T_m$	209.3	
Specific heat capacity (c_p)	$T < T_s^*$	711.2	J/(kg K)
	$T_s^* \leq\ T \leq\ T_l^*$	$\frac{711.2+937.4}{2} + \frac{L_m}{\delta\, T}$	
	$T > T_l^*$	937.4	
Viscosity (μ)	$T \leq\ T_s^*$	0.1	Kg/(m s)
	$T_s^* < T < T_l^*$	$0.1 - 0.09 * \frac{(T - T_s^*)}{\delta\, T}$	
	$T \geq\ T_l^*$	0.01	
Surface tension coefficient (σ)	$T > T_s^*$	$1.8 - 0.3 \times\ 10^{-3}\ (T - T_s^*)$	N/m
Marangoni coefficient ($d\sigma\ /dT$)		$0.3 \times\ 10^{-3}$	N/(m· K)
Energy absorption coefficient (α)		0.27	-

in which $A_t = 3000$, $B_t^* = 300$ and $r_t = 50$ µm. Figure 9 shows the tangential temperature gradients at the surface along with corresponding average ratios. For the modified kernel correction and the proposed new approach, since only the surface particles were included in the calculation of surface temperature gradients, the obtained results remain unchanged compared to those presented in Fig. 8. In contrast, the values estimated using the other approaches exhibit a decrease relative to the corresponding values in case test 2. In a real scenario, the temperature gradient at the surface typically presents a difference from that of the sub-surface. For this reason, accurately estimating the true surface temperature gradient through kernel gradient approximation becomes challenging due to the unified partition of smoothing kernel. When the incident laser beam intensity is relatively low in the simulations, such issue could be negligible, while numerical errors may be introduced when the simulations involve high laser intensity irradiation. Nevertheless, in the proposed method, since the surface temperature gradients are estimated by interpolating the temperature values of surface particles, such errors arising from the kernel gradient approximation can be eliminated. As a result, the proposed approach provides accurate approximations for the surface temperature gradients in all conducted tests.

6 Demonstration of the proposed scheme for laser material processing applications

Following the successful verification steps reported in the previous section, the proposed numerical framework for modelling melting pool dynamics was applied to specific applications of laser material processing, namely the laser micro texturing of a Ti6Al4V target first and then the laser powder bed fusion of 316 L stainless steel. It should be noted these simulations were conducted in 2D. Furthermore, by selecting appropriate artificial sound speed values, the maximum density error in the simulations was kept below 3%.

6.1 Laser micro texturing of Ti6Al4V

Figure 10 shows the initial computational domain of laser micro texturing, in which a Dirichlet temperature boundary condition of $T = 300$ K was enforced on the side and bottom surfaces of the workpiece using three layers of boundary particles (i.e., the surface with blue colouration in Fig. 10). Furthermore, heat loss due to convection, radiation and evaporation were considered for the top surface. The simulated results were compared against experimental data reported by Ma and co-workers who performed laser texturing operations on Ti6Al4V [27, 28]. The material

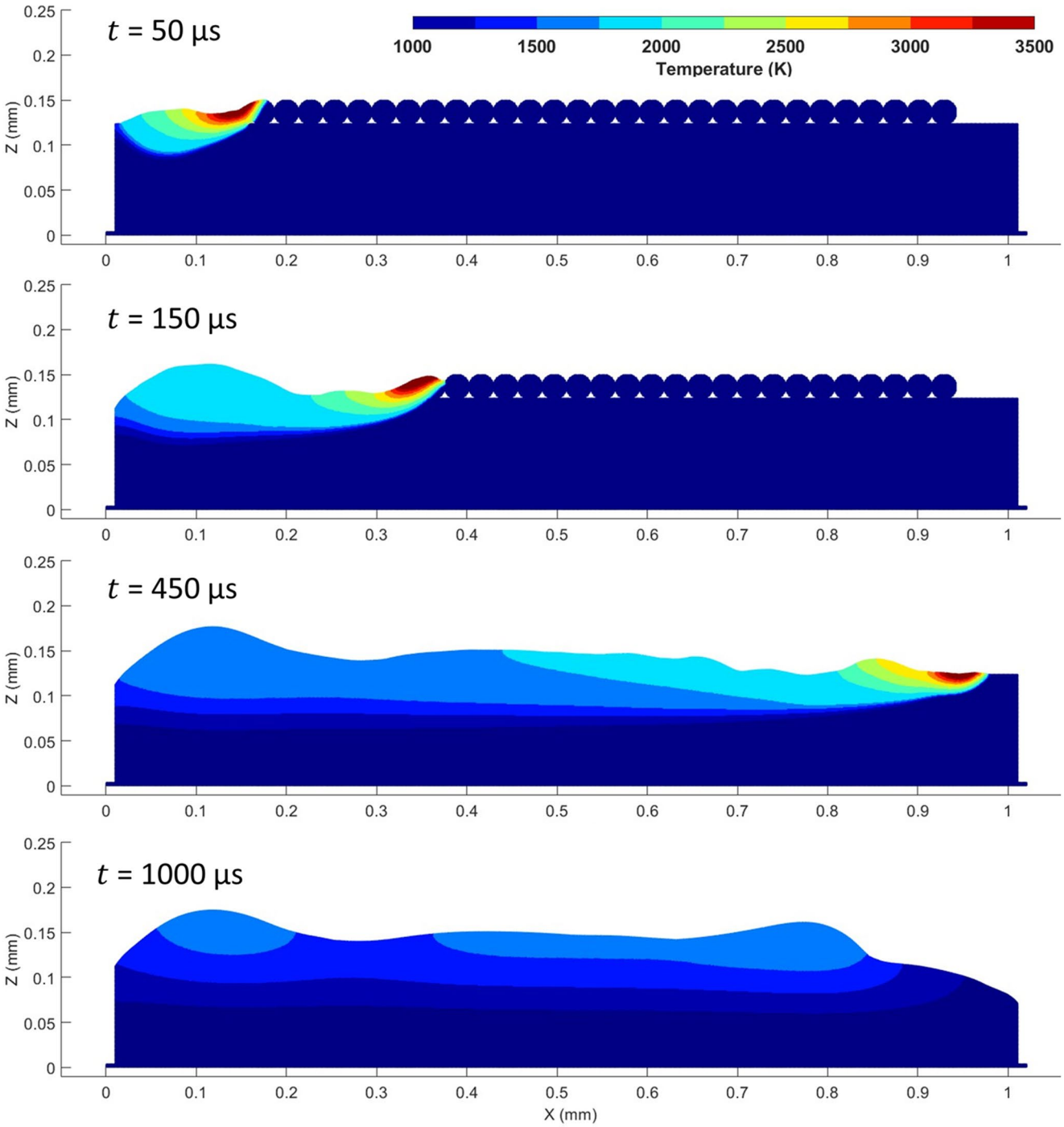

Fig. 16 Snapshots of the SPH simulated evolution in time of laser powder bed fusion for a laser power of 200 W and a scanning speed of 2 m/s

parameters of Ti6Al4V and the laser parameters used in this simulation are summarised in Table 3.

Among the material properties, the energy absorption coefficient α is key parameter. Since the energy absorption coefficient strongly depends on the reflectivity, its value could be estimated based on the reflectivity calculated from the Fresnel equation as [16, 50]:

$$R_l = \frac{[n_R - 1]^2 + n_I^2}{[n_R + 1]^2 + n_I^2}, \tag{64}$$

in which n_R and n_I are the real and imaginary parts of the refractive index, respectively. It was found the value of R_l is around 0.5 when the titanium target is irradiated by a laser with a wavelength of 1070 nm. Such calculated reflectivity is

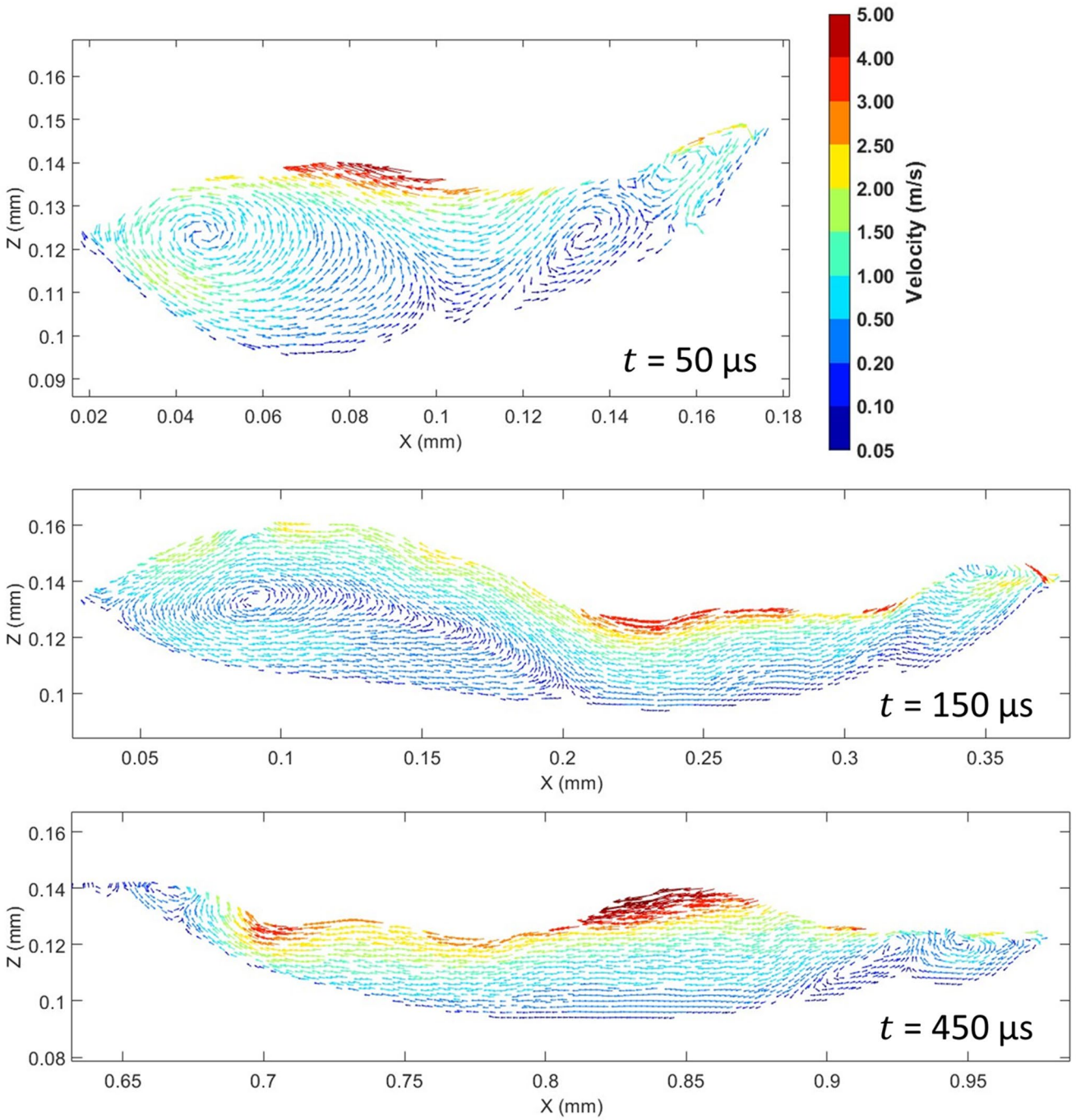

Fig. 17 The transient velocity fields of simulated laser powder bed fusion for a laser power of 200 W and a scanning speed of 2 m/s at $t = 50$, 150, and 450 µs

in good agreement with the value estimated in [27]. Hence, the energy absorption coefficient α was evaluated as (1-R_l), i.e., 0.5. As noted by the authors in [27], this value may have been underestimated in their conducted experimental scenario. Therefore, the energy absorption coefficient α is set slightly higher at 0.6 in this study. It is important to note such deviation from the calculated reflectivity is reasonable, as certain factors could influence its value in a specific experimental scenario, such as the surface oxides and surface roughness.

Figure 11 shows snapshots of the conducted simulation of laser micro texturing, with the temperature and velocity fields visualised simultaneously. Upon irradiation by the Gaussian laser, the target temperature increased, and melting began at around t =0.9 µs. With the further absorption of pulse energy, the size of melt pool gradually increases,

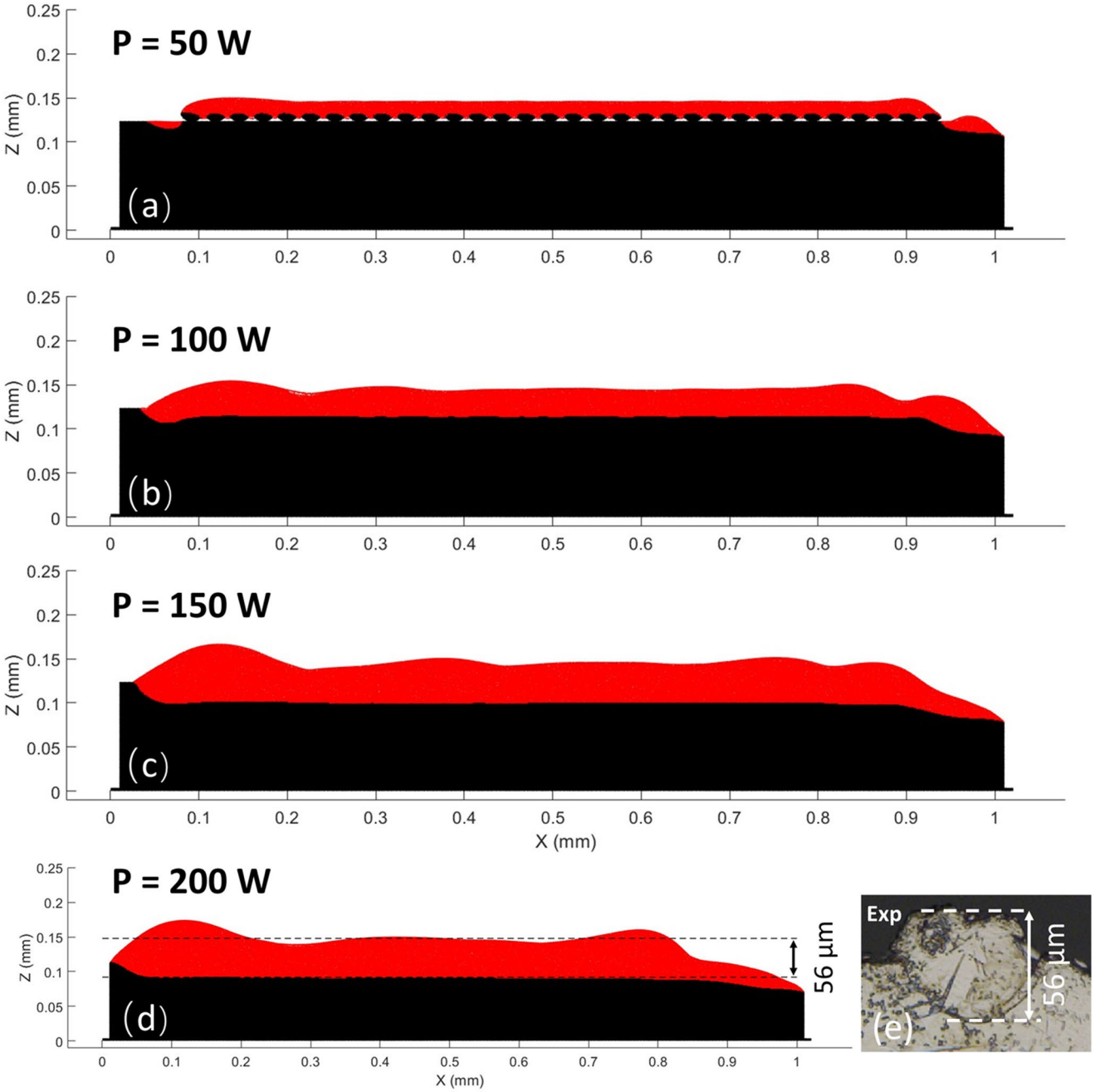

Fig. 18 **a–d** The simulated melt depths for laser powers ranging from 50 W to 200 W with a scanning speed of 2 m/s; **e** Experimentally measured melt depth for a laser power of 200 W and a scanning speed of 2 m/s. The experimental micrograph is reprinted from Khairallah and Anderson [29] Copyright (2025), with permission from Elsevier under License number 6035550637253

and the melted material is driven toward the edges of the melt pool due to the Marangoni force. At the end of the pulse, i.e., t =8.6 µs, the centre of melt pool reaches a peak temperature of approximately 3200 K. Although the laser pulse ends at t =8.6 µs, the size of the melt pool continues to increase due to heat conduction. Finally, the maximum melt pool depth is observed at around t =10 µs. In addition, the Marangoni convection effects (as shown at t =11 µs in Fig. 11) was found to become more significant during the cooling stage, whereas it is less prominent during the initial growth stage of melt pool (t <8.6 µs).

Figure 12a shows the simulated cooled melt pool shape in direct comparison with the experimentally measured shape obtained from [28]. It can be seen from this figure that the simulated melt pool profile is in very good agreement with the experimental cross section. In particular,

the simulated melt depth of 9.8 μm is closely aligned with the experimental value of 9.7±1.1 μm as reported in [27]. The simulated surface profile after solidification and corresponding experimental data are shown in Fig. 12b. Again, the simulated surface profile demonstrates good agreement with the experiment [28]. Specifically, the simulated peak-to-valley height of 4.4 μm closely matches with the experimental value of 4.5±0.4 μm as reported in [27].

To investigate the effects of recoil pressure, a simulation neglecting recoil pressure was also conducted. Figure 13 shows the simulated solidified surface profiles with and without the inclusion of recoil pressure. It can be observed that the peak-to-valley height was slightly reduced when the recoil pressure is excluded. Thus, the influence of the recoil pressure appears to be negligible in this case. This is likely due to the fact that the simulated temperature of the melt pool remained below the boiling point in this simulated laser texturing scenario. In contrast, the Marangoni force and surface tension emerged here as the primary factors influencing the generated crater size in laser micro texturing.

Figure 14 shows the simulated results of laser micro texturing using the developed SPH model compared to the Finite Element (FE) model reported in [27]. It can be observed that the proposed SPH model could provide more accurate predictions. The discrepancies between SPH and FE outcomes could be attributed to several factors, including the incorporated material model, thermal model, melting pool dynamics model and the numerical approach itself.

6.2 Laser powder bed fusion of 316 L stainless steel

In this section, the proposed framework was employed to model LPBF to further validate its implementation with a second laser material processing application. Figure 15 shows the computational domain of the developed SPH model of powder bed fusion, in which the particle size used in the simulations is 1 μm. A single-pass Gaussian laser beam was employed to scan the powder bed. As the Gaussian laser operates in a continuous wave model, the governing equation of laser source can be expressed as [29]:

$$Q_{laser} = \alpha\, A_g \frac{2P_{laser}}{\pi\, r_b^2} \exp\left(\frac{-2x^2}{r_b^2}\right), \tag{65}$$

where α is energy absorption coefficient, A_g is the top surface area of a grid cell in the implemented grid-based laser absorption scheme [16], p_{laser} is the laser power, r_b =27 μm is the laser beam radius. The powder particles had a diameter of 27 μm, and the material considered here was 316 L stainless steel, with its properties summarised in Table 4. In addition, a Dirichlet temperature boundary condition of $T = 300$ K was enforced on the bottom of the computational domain using three layers of boundary particles. The recoil pressure was not considered in these simulations.

Figure 16 shows the temperature snapshots of the simulated laser powder bed fusion with a laser power of 200 W and a scanning speed of 2 m/s. It can be observed that the molten material exhibits pronounced movement in the direction opposite to laser scanning, which is primarily induced by the Marangoni force. Since the magnitude of the Marangoni force significantly depends on the surface temperature gradient, a large surface temperature gradient in the melt pool can lead to a strong Marangoni effect. To further clarify the movement of the molten material, transient velocity fields at $t = 50$, 150, and 450 μs are presented in Fig. 17, in which significant Marangoni convection currents can be observed.

Figure 18a–d illustrate the simulated melt depths at laser power values ranging from 50 W to 200 W, with a scanning speed of 2 m/s. The molten particles are highlighted with red coloration. Figure 18d shows the experimentally measured melt depth at a laser power of 200 W and a scanning speed of 2 m/s, as reported in [29]. This cross-section micrograph was taken from the slices at peak position of the track. It can be said that the simulated melt depth demonstrates reasonably good agreement with experiment data. Similar SPH-based simulations of laser powder bed fusion have been conducted in previous studies [4, 7, 10]. However, these earlier SPH models could exhibit instability, as unrealistic particle ejections were observed in the simulations [4, 7, 10]. In contrast, the proposed scheme can provide stable and accurate simulated outcomes. Considering this, the proposed framework could be regarded as a viable new scheme for modelling laser powder bed fusion.

7 Conclusions

This paper presents a novel SPH-based numerical framework for modelling melting pool dynamics and its applications to laser micro texturing and laser powder bed fusion (LPBF). Conventional approaches for modelling melting pool dynamics were also reviewed briefly and considered for comparison purpose. To validate the accuracy of the proposed scheme, numerical test cases were carried out. It was found that the curvature and surface tangential temperature gradient estimated by the new approach could be more accurate than those obtained by conventional methods. In particular, conventional approaches to estimate surface temperature gradient could generate errors due to the truncated kernel support and unified partition of smoothing kernel. Furthermore, such errors could be more significant

in laser manufacturing, for which the temperature gradient at the surface exhibits a significant difference with the sub-surface.

Given the lack of particle-based numerical investigations in laser micro texturing, the proposed framework was applied for simulating this process and for exploring the potential of this particle-based modelling scheme. The main underlying physical factors of laser micro texturing were considered in the developed SPH model. These include temperature-dependent material properties, latent heat of phase transformation, recoil pressure, surface tension and Marangoni force. The Marangoni force and surface tension were found to be primary factors influencing the textured surface pattern, whereas the effects of recoil pressure were negligible due to the relatively low temperature of the melt pool in the scenario considered. Furthermore, the simulated melt pool shape and solidified surface profile were found to be in a good agreement with experimental data.

To further validate its accuracy and wider applicability, the framework was also implemented to model LPBF. In this case, numerically stable simulated outcomes were obtained. Under the effects of the Marangoni force, the molten material exhibited pronounced movement in the direction opposite to laser scanning, which resulted in significant Marangoni convection currents. The simulated melt depth demonstrated good agreement with experimental data. Given the successful implementation of numerical test cases and the demonstration with two specific applications, it is argued that the proposed SPH scheme can offer an accurate numerical framework for modelling melting pool dynamics for a wide range of laser material processing applications.

Acknowledgements Zhihao Zhong would like to acknowledge the support of the China Scholarship Council and Mr. Zebang Liu for the assistance with computational resources. This research was undertaken using the supercomputing facilities at Cardiff University operated by Advanced Research Computing at Cardiff (ARCCA) on behalf of the Cardiff Supercomputing Facility and the HPC Wales and Supercomputing Wales (SCW) projects. We acknowledge the support of the latter, which was part-funded by the European Regional Development Fund (ERDF) via the Welsh Government.

Author contributions Zhihao Zhong: Conceptualization, Methodology, Software, Visualization, Formal analysis, Writing– original draft. Sivakumar Kulasegaram: Methodology, Conceptualization, Formal analysis, Supervision, Writing– review & editing. Emmanuel Brousseau: Conceptualization, Formal analysis, Supervision, Writing– review & editing.

Data availability No datasets were generated or analysed during the current study.

Declarations

Competing interests The authors declare no competing interests.

References

1. Lucy LB (1977) A numerical approach to the testing of the fission hypothesis. Astron J 82:1013–1024
2. Gingold RA, Monaghan JJ (1977) Smoothed particle hydrodynamics: theory and application to non-spherical stars. Mon not R Astron Soc 181(3):375–389
3. Afrasiabi M, Bambach M (2023) Modelling and simulation of metal additive manufacturing processes with particle methods: a review. Virtual Phys Prototyp 18(1)
4. Russell MA, Souto-Iglesias A, Zohdi T (2018) Numerical simulation of laser fusion additive manufacturing processes using the SPH method. Comput Methods Appl Mech Eng 341:163–187
5. Ma Y, Zhou X, Zhang F, Weißenfels C, Liu M (2024) A novel smoothed particle hydrodynamics method for multi-physics simulation of laser powder bed fusion. Computat Mech 1–28
6. Fürstenau JP, Wessels H, Weißenfels C, Wriggers P (2020) Generating virtual process maps of SLM using powder-scale SPH simulations. Comput Part Mech 7(4):655–677
7. Afrasiabi M, Lüthi C, Bambach M, Wegener K (2021) Multi-resolution SPH simulation of a laser powder bed fusion additive manufacturing process. Appl Sci 11(7):2962
8. Dao MH, Lou J (2021) Simulations of laser assisted additive manufacturing by smoothed particle hydrodynamics. Comput Methods Appl Mech Eng 373:113491
9. Fuchs SL, Praegla PM, Cyron CJ, Wall WA, Meier C (2022) A versatile SPH modeling framework for coupled microfluid-powder dynamics in additive manufacturing: binder jetting, material jetting, directed energy deposition and powder bed fusion. Engineering with Computers 38(6):4853–4877
10. Long T, Huang H (2023) An improved high order smoothed particle hydrodynamics method for numerical simulations of selective laser melting process. Eng Anal Boundary Elem 147:320–335
11. Long T, Zhao Z (2024) An improved CSF model and an improved KGC technique incorporated in SPH for modeling selective laser melting process. Eng Anal Boundary Elem 167:105876
12. Weirather J, Rozov V, Wille M, Schuler P, Seidel C, Adams NA, Zaeh MF (2019) A smoothed particle hydrodynamics model for laser beam melting of Ni-based alloy 718. Comput Math Appl 78(7):2377–2394
13. Sollich D, Reinheimer EN, Wagner J, Berger P, Eberhard P (2022) An improved recoil pressure boundary condition for the simulation of deep penetration laser beam welding using the SPH method. Eur J Mechanics-B/Fluids 96:26–38
14. Muhammad N, Rogers BD, Li L (2013) Understanding the behaviour of pulsed laser dry and wet micromachining processes by multi-phase smoothed particle hydrodynamics (SPH) modelling. J Phys D 46(9):095101
15. Alshaer AW, Rogers BD, Li L (2017) Smoothed particle hydrodynamics (SPH) modelling of transient heat transfer in pulsed

laser ablation of al and associated free-surface problems. Comput Mater Sci 127:161–179
16. Zhong Z, Kulasegaram S, Brousseau E (2024) An enhanced meshless numerical methodology for modelling pulsed laser ablation of aluminium. J Manuf Process 131:1959–1969
17. Jiao Y, Brousseau E, Shen X, Wang X, Han Q, Zhu H, Bigot S, He W (2020) Investigations in the fabrication of surface patterns for wettability modification on a Zr-based bulk metallic glass by nanosecond laser surface texturing. J Mater Process Technol 283:116714
18. Tong W, Xiong D (2022) Direct laser texturing technique for metal surfaces to achieve superhydrophobicity. Mater Today Phys 23:100651
19. Melo-Fonseca F, Guimarães B, Gasik M, Silva FS, Miranda G (2022) Experimental analysis and predictive modelling of Ti6Al4V laser surface texturing for biomedical applications. Surf Interfaces 35:102466
20. Zhang J, Zhang S, Chen G, Jia Z, Qu Y, Guo Z (2022) Laser micro-texture formation mechanism based on modified heat-mass transfers and hydrodynamic models. Int J Mech Sci 230:107528
21. Abd-Elaziem W, Elkatatny S, Abd-Elaziem AE, Khedr M, Abd El-baky MA, Hassan MA, Abu-Okail M, Mohammed M, Järvenpää A, Allam T, Hamada A (2022) On the current research progress of metallic materials fabricated by laser powder bed fusion process: a review. J Mater Res Technol 20:681–707
22. Liu Z, Zhou Q, Liang X, Wang X, Li G, Vanmeensel K, Xie J (2024) Alloy design for laser powder bed fusion additive manufacturing: a critical review. Int J Extreme Manuf 6(2):022002
23. Soundararajan B, Sofia D, Barletta D, Poletto M (2021) Review on modeling techniques for powder bed fusion processes based on physical principles. Additive Manuf 47:102336
24. Morris JP (2000) Simulating surface tension with smoothed particle hydrodynamics. Int J Numer Methods Fluids 33(3):333–353
25. Vergnaud A, Oger G, Le Touzé D, DeLeffe M, Chiron L (2022) C-CSF: accurate, robust and efficient surface tension and contact angle models for single-phase flows using SPH. Comput Methods Appl Mech Eng 389:114292
26. Tong M, Browne DJ (2014) An incompressible multi-phase smoothed particle hydrodynamics (SPH) method for modelling thermocapillary flow. Int J Heat Mass Transf 73:284–292
27. Ma C, Vadali M, Duffie NA, Pfefferkorn FE, Li X (2013) Melt pool flow and surface evolution during pulsed laser micro polishing of Ti6Al4V. J Manuf Sci Eng 135(6):061023
28. Ma C, Vadali M, Duffie NA, Pfefferkorn FE, Li X (2013) Melt pool flow and surface evolution during pulsed laser micro polishing of Ti6Al4V. Int Manuf Sci Eng Conf 55454:V001T01A054. American Society of Mechanical Engineers
29. Khairallah SA, Anderson A (2014) Mesoscopic simulation model of selective laser melting of stainless steel powder. J Mater Process Technol 214(11):2627–2636
30. Liu MB, Liu G (2010) Smoothed particle hydrodynamics (SPH): an overview and recent developments. Arch Comput Methods Eng 17:25–76
31. Antuono M, Colagrossi A, Marrone S, Molteni D (2010) Free-surface flows solved by means of SPH schemes with numerical diffusive terms. Comput Phys Commun 181(3):532–549
32. Lind SJ, Xu R, Stansby PK, Rogers BD (2012) Incompressible smoothed particle hydrodynamics for free-surface flows: A generalised diffusion-based algorithm for stability and validations for impulsive flows and propagating waves. J Comput Phys 231(4):1499–1523
33. Monaghan JJ, Gingold RA (1983) Shock simulation by the particle method SPH. J Comput Phys 52(2):374–389
34. Brackbill JU, Kothe DB, Zemach C (1992) A continuum method for modeling surface tension. J Comput Phys 100(2):335–354
35. Cen C, Fourtakas G, Lind S, Rogers BD (2024) A single-phase GPU-accelerated surface tension model using SPH. Comput Phys Commun 295:109012
36. Marrone S, Colagrossi A, Le Touzé D, Graziani G (2010) Fast free-surface detection and level-set function definition in SPH solvers. J Comput Phys 229(10):3652–3663
37. Meier C, Fuchs SL, Hart AJ, Wall WA (2021) A novel smoothed particle hydrodynamics formulation for thermo-capillary phase change problems with focus on metal additive manufacturing melt pool modeling. Comput Methods Appl Mech Eng 381:113812
38. Lüthi C, Afrasiabi M, Bambach M (2023) An adaptive smoothed particle hydrodynamics (SPH) scheme for efficient melt pool simulations in additive manufacturing. Comput Math Appl 139:7–27
39. Monaghan JJ, Huppert HE, Worster MG (2005) Solidification using smoothed particle hydrodynamics. J Comput Phys 206(2):684–705
40. Wang Y, Shen N, Befekadu GK, Pasiliao CL (2017) Modeling pulsed laser ablation of aluminum with finite element analysis considering material moving front. Int J Heat Mass Transf 113:1246–1253
41. Gomez-Gesteira M, Rogers BD, Crespo AJ, Dalrymple RA, Narayanaswamy M, Dominguez JM (2012) SPHysics–development of a free-surface fluid solver–Part 1: theory and formulations. Comput Geosci 48:289–299
42. Monaghan JJ (1989) On the problem of penetration in particle methods. J Comput Phys 82(1):1–15
43. Monaghan JJ (2000) SPH without a tensile instability. J Comput Phys 159(2):290–311
44. Sun PN, Colagrossi A, Marrone S, Zhang AM (2017) The δplus-SPH model: simple procedures for a further improvement of the SPH scheme. Comput Methods Appl Mech Eng 315:25–49
45. Sun PN, Colagrossi A, Marrone S, Antuono M, Zhang AM (2019) A consistent approach to particle shifting in the δ-Plus-SPH model. Comput Methods Appl Mech Eng 348:912–934
46. Lyu HG, Sun PN (2022) Further enhancement of the particle shifting technique: towards better volume conservation and particle distribution in SPH simulations of violent free-surface flows. Appl Math Model 101:214–238
47. Monaghan JJ (1994) Simulating free surface flows with SPH. J Comput Phys 110(2):399–406
48. Rogers, B.D., Dalrymple, R.A., Gómez-Gesteira, M., Crespo, AJC. User guide for the parallelSPHysics code using MPI v2. 0, 2011. http://www.sphysics.org
49. Monaghan JJ (1992) Smoothed particle hydrodynamics. Ann Rev Astron Astrophys 30:543–574
50. Gragossian A, Tavassoli SH, Shokri B (2009) Laser ablation of aluminum from normal evaporation to phase explosion. J Appl Phys 105(10):103304
51. Zhang T, Li H, Liu S, Shen S, Xie H, Shi W, Zhang G, Shen B, Chen L, Xiao B, Wei M (2018) Evolution of molten pool during selective laser melting of Ti–6Al–4V. J Phys D 52(5):055302
52. Brillo J, Wessing J, Kobatake H, Fukuyama H (2019) Surface tension of liquid Ti with adsorbed oxygen and its prediction. J Mol Liq 290:111226
53. Yuan W, Chen H, Cheng T, Wei Q (2020) Effects of laser scanning speeds on different States of the molten pool during selective laser melting: simulation and experiment. Mater Design 189:108542